



Publication Year	2019
Acceptance in OA @INAF	2020-12-29T15:50:48Z
Title	The Formation Conditions of the Wide Binary Class 0 Protostars within BHR 71
Authors	Tobin, John J.; Bourke, Tyler L.; Mader, Stacy; Kristensen, Lars; Arce, Hector; et al.
DOI	10.3847/1538-4357/aaef87
Handle	http://hdl.handle.net/20.500.12386/29297
Journal	THE ASTROPHYSICAL JOURNAL
Number	870



The Formation Conditions of the Wide Binary Class 0 Protostars within BHR 71

John J. Tobin^{1,2,13} , Tyler L. Bourke³, Stacy Mader⁴, Lars Kristensen⁵ , Hector Arce⁶ , Frédéric Gueth⁷, Antoine Gusdorf⁸, Claudio Codella^{9,10} , Silvia Leurini¹¹, and Xuepeng Chen¹²

¹ Homer L. Dodge Department of Physics and Astronomy, University of Oklahoma, 440 W. Brooks Street, Norman, OK 73019, USA; jtobin@nrao.edu

² Leiden Observatory, Leiden University, P.O. Box 9513, 2300-RA Leiden, The Netherlands

³ SKA Organization, Jodrell Bank Observatory, Lower Withington, Macclesfield, Cheshire SK11 9DL, UK

⁴ CSIRO Astronomy and Space Sciences, Parkes Observatory, P.O. BOX 276, Parkes NSW 2870, Australia

⁵ Centre for Star and Planet Formation, Niels Bohr Institute and Natural History Museum of Denmark, Copenhagen University, Øster Voldgade 5–7, DK-1350 Copenhagen K, Denmark

⁶ Department of Astronomy, Yale University, P.O. Box 208101, New Haven, CT 06520-8101, USA

⁷ Institut de Radioastronomie Millimétrique (IRAM), F-38406 Saint-Martin d'Hères, France

⁸ LERMA, Observatoire de Paris, École normale supérieure, PSL Research University, CNRS, Sorbonne Universités, UPMC Univ. Paris 06, F-75231, Paris, France

⁹ INAF, Osservatorio Astrofisico di Arcetri, Largo E. Fermi 5, I-50125 Firenze, Italy

¹⁰ Univ. Grenoble Alpes, Institut de Planétologie et d'Astrophysique de Grenoble (IPAG), F-38401 Grenoble, France

¹¹ INAF - Osservatorio Astronomico di Cagliari, Via della Scienza 5, I-09047 Selargius (CA), Italy

¹² Purple Mountain Observatory, Chinese Academy of Sciences, Nanjing 210034, People's Republic of China

Received 2018 July 30; revised 2018 October 29; accepted 2018 November 6; published 2019 January 10

Abstract

We present a characterization of the binary protostar system that is forming within a dense core in the isolated dark cloud BHR71. The pair of protostars, IRS1 and IRS2, are both in the Class 0 phase, determined from observations that resolve the sources from 1 μm out to 250 μm and from 1.3 mm to 1.3 cm. The resolved observations enable the luminosities of IRS1 and IRS2 to be independently measured (14.7 and 1.7 L_{\odot} , respectively), in addition to the bolometric temperatures 68 K and 38 K, respectively. The surrounding core was mapped in NH_3 (1, 1) with the Parkes radio telescope, and followed with higher-resolution observations from ATCA in NH_3 (1, 1) and 1.3 cm continuum. The protostars were then further characterized with ALMA observations in the 1.3 mm continuum along with N_2D^+ ($J = 3 \rightarrow 2$), ^{12}CO , ^{13}CO , and C^{18}O ($J = 2 \rightarrow 1$) molecular lines. The Parkes observations find evidence for a velocity gradient across the core surrounding the two protostars, while ATCA reveals more complex velocity structure toward the protostars within the large-scale gradient. The ALMA observations then reveal that the two protostars are at the same velocity in C^{18}O , and N_2D^+ exhibits a similar velocity structure as NH_3 . However, the C^{18}O kinematics reveal that the rotation on scales < 1000 au around IRS1 and IRS2 are in *opposite* directions. Taken with the lack of a systematic velocity difference between the pair, it is unlikely that their formation resulted from rotational fragmentation. We instead conclude that the binary system most likely formed via turbulent fragmentation of the core.

Key words: ISM: individual objects (BHR71) – ISM: kinematics and dynamics – ISM: molecules – stars: formation – stars: protostars – techniques: interferometric

1. Introduction

Binary and multiple star systems are a frequent outcome of the star formation process at both low and high masses (e.g., Raghavan et al. 2010; Duchêne & Kraus 2013). While the statistics of multiple star formation in the main-sequence and pre-main sequence phase and even the protostellar phase are becoming much better characterized (Raghavan et al. 2010; Kraus et al. 2011; Chen et al. 2013; Ward-Duong et al. 2015; Tobin et al. 2016), the physical processes that lead to multiple star formation are not well characterized observationally. The main epoch of multiple star formation is the protostellar phase (Tohline 2002; Chen et al. 2013), when the protostar(s) are surrounded by a dense infalling cloud(s) of gas and dust. Thus, it is imperative to examine the process of multiple star formation in the protostellar phase with a combination of continuum and molecular line tracers to reveal the physical processes at work.

While it is essential to examine multiple star formation in the protostellar phase, star formation typically occurs in clusters

(e.g., Lada & Lada 2003; Megeath et al. 2012), which increases the complexity of the data, especially for spectral line tracers that reveal the motion of gas along the line of sight. Toward small proto-clusters in molecular clouds (e.g., NGC 1333), complex motions of the surrounding gas can complicate the interpretation of kinematic data, making multiple star formation difficult to characterize. Thus, stars forming in nearby isolated clouds, the so-called Bok globules, can be valuable laboratories for the study of multiple star formation. This is especially true for wide multiple star systems, where separations are greater than 1000 au, because the kinematics should be less confused along the line of sight. The BHR71 system (Bourke et al. 1995a; Bourke 2001; Chen et al. 2008; Yang et al. 2017) is composed of two Class 0 protostars (André et al. 1993) separated by $\sim 16''$ (3200 au; 200 pc distance), and it is an ideal system to study the physics of wide multiple star formation. The fact that both components of the binary system are in the Class 0 phase means that the protostars are very young, likely younger than ~ 150 kyr (Dunham et al. 2014). Therefore, the initial conditions of their formation are not likely to have been erased by the dynamical interactions of the protostars and their effects on the surrounding cloud from their outflows (Arce & Sargent 2006).

¹³ Current Address: National Radio Astronomy Observatory, 520 Edgemont Road, Charlottesville, VA 22903, USA.

The formation of wide multiple star systems has been thought to be related to the rotation of the infalling envelope of the protostar, where greater rotation rates would lead to an increased likelihood of fragmentation. Many theoretical and numerical studies have highlighted the importance of rotation in the formation of wide and close multiple star systems (Larson 1972; Burkert & Bodenheimer 1993; Boss 1995, 2002; Boss & Keiser 2013). The importance of rotation is typically parametrized as β_{rot} which is the ratio of rotational energy to gravitational potential energy. Chen et al. (2012) compiled a list of all known single and multiple protostars and calculated their β_{rot} values, finding that most binary/multiple protostars have $\beta_{\text{rot}} > 0.01$. However, β_{rot} is observationally derived from measurement of velocity gradients in the cores/envelopes surrounding the protostar(s), and Tobin et al. (2011, 2012a) highlighted the possibility that these velocity gradients may not truly reflect rotation due to the possibility of large-scale asymmetries in the envelope structures (Tobin et al. 2010b) and filamentary structure (e.g., André et al. 2010; Hacar & Tafalla 2011). Furthermore, numerical simulations of star formation in turbulent molecular clouds have shown that the turbulence can lead to the formation of multiple star systems on ~ 1000 au scales (Padoan & Nordlund 2002; Offner et al. 2010), possibly removing the need for bulk envelope rotation to initiate multiple star formation. Therefore sensitive molecular line data tracing the gas kinematics are required, spanning orders of magnitude in spatial scales to differentiate between different scenarios of multiple star formation.

We have obtained a comprehensive data set on BHR71 spanning the scales of the star-forming core at $\sim 1'$ (12,000 au) resolution down to $1''.5$ (300 au) to examine the full range of scales within this isolated binary protostar system. With this data set, we aim to determine what physical process(es) lead to the formation of at least two protostars in this system. The results will be useful for interpreting observations of more evolved multiple star systems and other forming multiple systems. The data set includes *Herschel* photometry, Australia Telescope Compact Array (ATCA) continuum and molecular line observations, Parkes Radio Telescope NH_3 line mapping, and Atacama Large Millimeter/submillimeter Array (ALMA) observations of continuum and molecular lines. The paper is organized as follows: the observations are presented in Section 2, the observational results regarding classification, photometry, and continuum are presented in Section 3, the result from the continuum and molecular line data are presented in Section 4, the results are discussed in Section 5, and our conclusions are presented in Section 6.

2. Observations

2.1. Parkes Radio Telescope

We observed BHR71 with the Parkes 64 m radio telescope on 2012 September 06 (project P825). The 13 mm receiver was used and we observed an on-the-fly (OTF) map of BHR71 covering an $8' \times 8'$ area surrounding BHR71 in the NH_3 (1, 1) transition using dual polarization. The usable surface of the Parkes dish is 55 m at 1.3 cm, resulting in a beam size of $\sim 60''$, see Table 1 for a summary. The weather was good and T_{sys} was ~ 100 K. The observations were conducted shortly after the 13 mm receiver was mounted. An all-sky pointing model could not be completed prior to our observations. We instead used a local pointing solution on the nearby quasar 1057-797.

The flux calibration of the data was done using the quasar 1057-797, which was the gain calibrator for the ATCA observations that were conducted a few days before (see below). The data were reduced using the *livedata* and *gridzilla* tasks within AIPS++. The *livedata* task was used to perform baseline subtraction and scaling to the proper flux density of each spectrum in the map, while *gridzilla* was used to construct a datacube from the individual spectra in FITS format. After mapping the data, we realized that there was a systematic offset in the central coordinates of the map; BHR71 was located $\sim 1'$ north of the pointing center. The systematic offset likely resulted from the lack of an all-sky pointing solution prior to the observations. To recenter the map, we smoothed the ATCA data to the same resolution as the Parkes data and matched the peak emission of the core. Given that some emission is resolved out in the ATCA observations, there is likely some residual pointing uncertainty of the map on the order of $15''$ to $20''$.

The FITS cube was then ingested into CLASS, which is part of the GILDAS¹⁴ software package, using the CLASS function *lmv*. We then used the built-in NH_3 line-fitting functions to construct the centroid velocity maps and the line-width maps.

2.2. ATCA Observations

BHR71 was observed with ATCA during 2012 in the EW367 configuration and H214 configuration, project C2665. ATCA consists of six antennas that are 22 meters in diameter. One antenna is fixed on a pad 6 km from the array center, the remaining five antennas are reconfigurable on an east–west track and a shorter north–south track. In both observations, we targeted the NH_3 (1, 1), (2, 2), and (3, 3) inversion transitions at 23.694, 23.722, and 23.870 GHz. The primary beam of the 22 m antennas at these frequencies is $\sim 144''$. The observations are summarized in Table 1.

The Compact Array Broadband Backend (CABB) correlator was used for our observations, providing 2 GHz of continuum bandwidth (with 2048 channels, 1 MHz wide each), and we placed 1 MHz zoom bands, each with 2048 channels (0.5 kHz channels) at the frequencies of the NH_3 (1, 1), (2, 2), and (3, 3) inversion transitions. We used six zoom bands each for NH_3 (1, 1) and (2, 2), and four zoom bands for NH_3 (3, 3). We used 1057-797 as the complex gain calibrator, 0537-441 as the bandpass calibrator, and 1934-638 was the flux calibrator for both the H214 and EW367 observations.

We observed BHR71 on 2012 April 22 in the EW367 configuration, where the maximum baseline is 367 meters with all antennas positioned along the east–west track; the shortest baseline was ~ 38 meters. The weather conditions were variable during the observation with T_{sys} typically ~ 100 K. The observations were conducted for a full 12 hr synthesis track. However, there was rain during the last two hours of the observations, and data from that time period were unusable. The observations were conducted as a seven-point mosaic where the goal was to obtain a constant surface brightness sensitivity over the central $\sim 144''$ primary beam. However, due to an error in the mosaic setup, the mosaic was not as wide in the right ascension direction as intended. This did not adversely affect the sensitivity of our map because the NH_3 emission from BHR71 was adequately mapped with this mosaic pattern.

¹⁴ <http://www.iram.fr/IRAMFR/GILDAS>

Table 1
Molecular Line Setups

Telescope	Molecule	Frequency (GHz)	Raw Spectral Resolution (kHz, km s ⁻¹)	Map Spectral resolution (km s ⁻¹)	Map rms (Jy beam ⁻¹ or K)	Beam (″)	Detected?
Parkes	NH ₃ (1, 1)	23.694495	1.0, 0.012	0.05	0.1 K	60	Y
ATCA	NH ₃ (1, 1)	23.694495	0.5, 0.006	0.1	0.015 Jy beam ⁻¹ , 0.19 K	9.1 × 7.8	Y
	NH ₃ (2, 2)	23.722633	0.5, 0.006	0.2	0.012 Jy beam ⁻¹	10.8 × 9.2	M
	NH ₃ (3, 3)	23.870129	0.5, 0.006	0.2	0.011 Jy beam ⁻¹	10.8 × 9.2	N
	Continuum	23.160	1.0, 13.0	...	0.000048 Jy beam ⁻¹	9.4 × 8.1	Y
ALMA	C ¹⁸ O ($J = 2 \rightarrow 1$)	219.560354	61.035, 0.083	0.083	0.029 Jy beam ⁻¹	1.7 × 1.5	Y
	¹³ CO ($J = 2 \rightarrow 1$)	220.398684	61.035, 0.083	0.083	0.035 Jy beam ⁻¹	1.7 × 1.4	Y
	¹² CO ($J = 2 \rightarrow 1$)	230.538	61.035, 0.079	0.166	0.029 Jy beam ⁻¹	1.5 × 1.3	Y
	N ₂ D ⁺ ($J = 3 \rightarrow 2$)	231.321828	61.035, 0.079	0.083	0.034 Jy beam ⁻¹ , 0.23 K	2.0 × 1.8	Y
	Continuum	232.5	14.6, 18.8	...	0.00087 Jy beam ⁻¹	1.3 × 1.2	Y

Note. The final column, with the label “Detected?”, denotes whether the molecule or continuum was detected with high confidence (Y), is a marginal detection (M), or is a non-detection (N).

BHR71 was also observed on 2012 September 24 with ATCA in the H214 configuration, where five antennas were positioned along the north–south track with a shortest baseline length of ~ 47 meters. The observing track length was 8 hr and T_{sys} was ~ 80 K throughout the observations. The weather conditions were good and the phase between antennas was stable during the observations. These observations were also conducted in a seven-point mosaic, with uniform coverage of the central $\sim 144''$.

The data were calibrated and edited using the Australian Telescope National Facility (ATNF) version of the MIRIAD software package (Sault et al. 1995). The phases and amplitudes for each baseline were inspected and edited to remove periods of high phase-noise and/or amplitude deviations. We also flagged the single antenna on the 6 km baseline because of high phase-noise and lack of uv coverage at intermediate baselines.

The combined EW367 and H214 data sets were imaged using the *clean* algorithm implemented in MIRIAD. We generated both a 1.3 cm continuum image of BHR71 and channel maps centered on the NH₃ (1, 1), (2, 2), and (3, 3) transitions; however, only the NH₃ (1, 1) line was well detected. We did not combine the ATCA and Parkes data due to the positional uncertainty in the Parkes data. We instead used them independently for the spatial scales they are sensitive to.

2.3. ALMA Observations

BHR71 was observed by the ALMA 12 m array, the ALMA Compact Array (ACA), and the Total Power Array (TPA) under the project 2013.1.00518.S. The observations were conducted in band 6, with a central tuning frequency of 225 GHz. In all observations, the correlator was configured to observe ¹²CO ($J = 2 \rightarrow 1$), ¹³CO ($J = 2 \rightarrow 1$), C¹⁸O ($J = 2 \rightarrow 1$), N₂D⁺ ($J = 3 \rightarrow 2$), and continuum. The continuum basebands were located at 232.5 GHz, a region without many significant spectral lines, and 218 GHz. The 218 GHz band had significant contamination from spectral lines and was not used for continuum measurements. The continuum bands were observed in TDM mode, with 128 channels over the 2 GHz of bandwidth each. ¹²CO and N₂D⁺ were observed in the same baseband, with each having 58 MHz of bandwidth and 1920 channels, providing a velocity resolution of ~ 0.08 km s⁻¹. ¹³CO and C¹⁸O were also observed in the

same baseband with identical bandwidth and velocity resolution. See Table 1 for a summary of the observational setup.

The 12 m array observations were conducted on 2015 January 17 in a 14-point rectangular mosaic with 34 antennas operating, covering a $45'' \times 45''$ region centered between the two protostars. The precipitable water vapor (PWV) was 3.64 mm at the time of execution. Each mosaic point was observed for ~ 62 s and the complete scheduling block was executed in ~ 44 minutes. The observations were manually calibrated by T. Hunter at the North American ALMA Science Center (NAASC) using CASA version 4.3.1, and we used the provided reduction script to generate the calibrated data products. We then self-calibrated the data using the observed dust continuum; not all mosaic points contained a detection of the continuum source, therefore self-calibration was only applied to the mosaic points where the continuum was detected. We performed both phase and amplitude self-calibration on the data. The refined phase and amplitude solutions were then applied to the spectral line basebands. The data were then imaged using the *clean* task in CASA 4.4. We used interactive cleaning for the continuum and spectral line cubes. For the spectral line data, we manually drew masks around the emission in each velocity channel and refined the mask when needed after each iteration of *clean*.

The ACA observations were conducted on 2014 May 19 in a five-point mosaic centered between the two protostars. The observation took ~ 50 minutes and nine antennas were operating. Each mosaic point was observed for 74 s and the science observations had a total of 12.3 minutes on-source. The PWV during these observations was 0.7 mm. These data were calibrated by B. Mason at the NAASC using the ALMA pipeline and CASA version 4.2.2, and we used the reduction script to regenerate the calibrated data product. We also self-calibrated these data. All mosaic points contained the continuum source due to the larger primary beam of the 7 m antennas. The refined phase and amplitude solutions from the continuum were then applied to the spectral line data. The data were imaged using the *clean* task in interactive mode following the same method as outlined for the 12 m data.

The TPA observations were conducted on 2015 May 2, in three executions of ~ 57 minutes each, observing a $93''6 \times 93''6$ on-the-fly (OTF) map using two TPA antennas. The PWV at the time of execution was 0.9 to 1.3 mm. We found that the pipeline-reduced data did not adequately fit the spectral baseline of the ¹²CO data due to the broad line width. We re-ran the reduction script in CASA version 4.3.1 and

manually adjusted the region to fit the spectral baseline in order to avoid the high-velocity ^{12}CO emission.

We then combined the ^{12}CO , ^{13}CO , C^{18}O , and N_2D^+ data using the methods outlined in the CASA guide for M100 using CASA version 4.6.0.¹⁵ The 12m+ACA visibilities were combined using the *concat* task in CASA, with the weights being properly adjusted by CASA to compensate for the lower sensitivity of the ACA data. We used the *clean* task to image the combined data set in the same manner as the individual data sets. We then followed the CASA guide for M100 to combine the 12m+ACA and TPA data using the *feather* task. The fully combined spectral line data set had significantly reduced artifacts for all molecules where there was significant extended emission. We make use of the fully combined data (12m+ACA+TPA) in this paper, except for two C^{18}O position-velocity (PV) diagrams, and this is noted in the text and caption. Furthermore, the continuum maps are only 12m+ACA because total power data are not available.

2.4. Magellan PANIC Observations

We observed BHR71 with the *Magellan* Baade 6.5 m telescope located at Las Campanas using the Persson's Auxiliary Nasmyth Infrared Camera (PANIC; Martini et al. 2004) near-infrared imager on 2009 January 17 and 18. The PANIC instrument uses a 1024^2 detector with $0''.12$ pixels, providing a $2' \times 2'$ field of view. The observations for BHR71 were previously presented in Tobin et al. (2010a), and we only observed *H* and *Ks* bands with this instrument. The seeing was exceptional during these observations at $\sim 0''.4$.

2.5. Cerro-Tololo ISPI Observations and Photometry

We observed BHR71 using the Infrared Side-Port Imager (ISPI; van der Blik et al. 2004) on the Blanco 4 m telescope at Cerro-Tololo on 2009 June 11. The ISPI observations and data reduction were described in detail in Tobin et al. (2010a), and the imager has a $10'$ field of view with a 2048^2 detector. We use the *J*, *H*, and *Ks*-band images from ISPI for near-infrared photometry in this paper because the field of view is larger than that of PANIC. Moreover, the absolute calibration of the ISPI data is expected to be more robust because more stars are available for calibration against 2MASS (Skrutskie et al. 2006). We measured the photometry in the *J*, *H*, and *Ks* bands using a circular aperture radius of $30''$ (6000 au) for IRS1 and a $5''$ (1000 au) radius for IRS2. IRS2 was undetected in this aperture. The background was measured using the median of an off-source patch of sky given the highly extended nature of the scattered light emission. The data were calibrated using photometry from the 2MASS catalog (Skrutskie et al. 2006), and the photometry is listed in Table 2. The seeing during these observations was $\sim 0''.9$.

2.6. Spitzer Observations and Photometry

BHR71 was observed with the *Spitzer Space Telescope* using the IRAC (Fazio et al. 2004), MIPS (Rieke et al. 2004), and IRS instruments (Houck et al. 2004). The IRAC and MIPS observations were part of the *cores2disks* Legacy program, and the reduced data were obtained from the *cores2disks* data archive. The IRS observations were obtained as part of the IRS guaranteed time program and previously published in Yang

et al. (2017). The MIPS $24\ \mu\text{m}$ photometry for IRS1 and IRS2 was presented in Chen et al. (2008), and we re-extracted the IRAC photometry of the extended scattered light nebulae toward BHR71 IRS1 and IRS2 at 3.6, 4.5, 5.8, and $8.0\ \mu\text{m}$ using same the methods as outlined for the protostar BHR7-MMS in Tobin et al. (2018). We extracted the photometry from a 6000 au ($30''$) radius aperture toward IRS1 and a 1000 au ($5''$) aperture radius toward IRS2. The 6000 au aperture for IRS1 includes flux from IRS2, but the contribution is at most $\sim 10\%$ (see Table 2). We also extracted the photometry from a 10,000 au radius ($50''$) centered on IRS1. We chose these apertures as they are convenient fiducial values and radiative transfer models offer the option to extract flux within different apertures around the source(s) (e.g., Whitney et al. 2003). The 1000 au aperture restricts the scattered light emission to a region close to the source and is less affected by the source structure; the 6000 au and 10,000 au apertures are useful for characterizing the total flux density of scattered light from the source(s). Because contributions from IRS2 at wavelengths shorter than $24\ \mu\text{m}$ are small, we decided to extract the large apertures for IRS1 in addition to the small uncontaminated apertures.

2.7. Herschel Observations and Photometry

We obtained the *Herschel* observations toward BHR71 as part of the program OT1_jtobin_1. BHR71 was observed with the PACS photometer (Poglitsch et al. 2010) on 2011 July 28. The 100 and $160\ \mu\text{m}$ maps were obtained simultaneously with a map size of $10' \times 10'$, observing two orthogonal scans for 18.5 minutes each. The $70\ \mu\text{m}$ data were obtained separately, mapping a smaller, $2' \times 2'$ region, also observing two orthogonal scans for 14.4 minutes each. Both sets of PACS observations were made using the medium scan speed ($20''$ per minute) for best image quality. The SPIRE (Griffin et al. 2010) observations were obtained as part of the same program as the PACS observations on 2011 August 16. We observed a $10' \times 10'$ region around the protostars with orthogonal scan legs for a total time of 17.25 minutes. In our subsequent analyses, we used the Jscanam¹⁶ products downloaded from the *Herschel* Science Archive.

We performed photometry on the PACS and SPIRE data using both aperture photometry and point-spread function (PSF) photometry. At 70, 100, 160, and $250\ \mu\text{m}$, we used PSF photometry to measure the flux densities toward both IRS1 and IRS2. The sources are significantly blended at wavelengths longer than $100\ \mu\text{m}$ and are within the PSF wings of each other at 70 and $100\ \mu\text{m}$. We used the IDL program *starfinder* (Diolaiti et al. 2000) to perform PSF photometry. Because the mapped region is small, we could not measure the PSF from the data. Instead, we used the Vesta PSF measurements from the pointing-refined data that we then rotated and smoothed to match the data. This enabled us to measure the photometry toward the two sources, with the positions being automatically fit at 70, 100, and $160\ \mu\text{m}$. Owing to the increased blending at $250\ \mu\text{m}$, we specified the positions for the two sources that were identified at shorter wavelengths and extracted the $250\ \mu\text{m}$ photometry. No other sources lie in the field, therefore we were unable to cross-calibrate our PSF photometry with aperture photometry to verify its accuracy. However, the

¹⁵ https://casaguides.nrao.edu/index.php/M100_Band3_Combine_5.1

¹⁶ This is a port of the Scanamorphos map making software (Roussel 2013) into the *Herschel* Interactive Processing Environment (HIPE).

Table 2
Photometry

Wavelength (μm)	IRS1 Flux Density (Jy)	IRS2 Flux Density (Jy)	Total Flux Density (Jy)	Instrument	Resolution ($''$)	Aperture Radius ^a ($''$)	References
1.25	0.0048 ± 0.0005	$<1.4\text{e-}4$	0.017 ± 0.0017	CTIO/ISPI	0.9	30, 5, 50	1
1.66	0.025 ± 0.006	$<2.6\text{e-}4$	0.072 ± 0.007	CTIO/ISPI	0.9	30, 5, 50	1
2.15	0.14 ± 0.014	$<2.5\text{e-}3$	0.33 ± 0.03	CTIO/ISPI	0.9	30, 5, 50	1
3.6	0.073 ± 0.07	0.0045 ± 0.0004	0.15 ± 0.02	IRAC	1.7	30, 5, 50	1
4.5	0.15 ± 0.02	0.012 ± 0.007	0.27 ± 0.015	IRAC	1.7	30, 5, 50	1
5.8	0.17 ± 0.02	0.015 ± 0.007	0.27 ± 0.004	IRAC	1.8	30, 5, 50	1
8.0	0.14 ± 0.03	0.009 ± 0.0006	0.17 ± 0.08	IRAC	1.9	30, 5, 50	1
24.0	5.0 ± 0.3	0.09 ± 0.003	5.1 ± 0.3	MIPS	6	PSF, PSF, 50	2
60.0	77.4 ± 15.5	IRAS	72	300	3
70.0	127.2 ± 12.7	8.8 ± 1.0	145.7 ± 14.5	PACS	5.6	PSF, PSF, 50	1
100.0	230.9 ± 23.0	22.8 ± 4.1	292.7 ± 30.0	PACS	6.8	PSF, PSF, 50	1
160.0	248.4 ± 25.0	37.6 ± 8.0	353.8 ± 35.0	PACS	10.7	PSF, PSF, 50	1
250.0	157.5 ± 30.0	36.1 ± 6.0	213.4 ± 22.0	SPIRE	18	PSF, PSF, 22	1
350.0	127.0 ± 9.1	SPIRE	24	30	1
500.0	64.8 ± 4.5	SPIRE	35	40	1
1300.0	3.8 ± 0.72	SEST	23	60	4
1300.0	1.28 ± 0.01	0.12 ± 0.005	1.41 ± 0.016	ALMA	1.25	12.5, 5, 17.5	1
3200.0	0.140 ± 0.028	0.0028 ± 0.0021	0.143 ± 0.028	ATCA	3.5	Gaussian	2
12960.0	0.0027 ± 0.0002	0.00022 ± 0.0001	0.0029 ± 0.0002	ATCA	9	Gaussian	1

Notes. The flux density for IRS1 includes a minor contribution from IRS2 because the $30''$ (6000 au) radius aperture comes close to encompassing the system. The total flux density refers to the flux measured in the third aperture listed in the Aperture column. References: (1) This work; (2) Chen et al. (2008); (3) IRAS photometry; (4) Launhardt et al. (2010).

^a The values separated by commas in this column represent the aperture used for IRS1, IRS2, and the their combined flux densities, respectively. The aperture for the combined flux densities of IRS1 and IRS2 is chosen to encompass the emission of both sources. The numerical sizes denote aperture photometry, PSF denotes photometry by point-spread function fitting, and Gaussian denotes photometry by Gaussian fitting.

Herschel Orion Protostar Survey (HOPS) used both aperture and PSF photometry and found close agreement between the two (Furlan et al. 2016). The flux density measured using PSF photometry is expected to be systematically lower than the aperture photometry because aperture photometry includes additional extended emission surrounding the sources. PSF photometry from PACS has been characterized by B. Ali et al. (2018, in preparation) for the HOPS protostars (e.g., Furlan et al. 2016), finding that the PSF photometry either agrees with the aperture photometry or is systematically low as a result of additional extended flux in the aperture photometry. Magnelli et al. (2013) also used PSF photometry, but created empirical PSFs from their data that were truncated to avoid including the full PSF wings. This caused their photometry to be systematically low, $\sim 70\%$ of the aperture measurement at $160 \mu\text{m}$. However, we used the full Vesta PSF to fit our data and do not expect this systematic effect in our measurements.

To measure the aperture photometry, we used $40''$ radius apertures at 70, 100, and $160 \mu\text{m}$, centered between the two protostars. We chose different apertures for the *Herschel* PACS photometry in comparison to the shorter wavelength photometry because the aperture and color corrections are tabulated for this aperture. We also corrected for the encircled energy fraction as documented in the PACS Data Handbook. The summed PSF photometry of IRS1 and IRS2 is about 20% lower than the aperture photometry at each wavelength, which is reasonable because the PSF photometry excludes the extended emission surrounding the sources.

For the SPIRE photometry, we used standard apertures of $22''$, $30''$, and $40''$ for the 250, 350, and $500 \mu\text{m}$ bands, respectively. These apertures are again different from other wavelengths because their aperture and color corrections are tabulated. We started with the extended source map and used

the tabulated beam correction, color correction, and aperture correction for a source with a spectral index of 3.5 and a temperature of 30 K. These are reasonable assumptions for a protostar as the spectral energy distribution (SED) peaks at $\sim 100 \mu\text{m}$ and the dust opacity spectral index will result in a spectral index between 3 and 4 in the submillimeter range. Our photometry is taken toward the region of compact emission toward the protostar locations and not from the entire extended core; therefore a proper zero-point flux calibration as in Sadavoy et al. (2018) is not required.

3. Observational Results

The multitude of infrared and submillimeter data taken toward BHR71 are shown in Figures 1 and 2. Figure 1 shows the high-resolution ground-based near-infrared view, the *Spitzer* IRAC view, and the mid- to far-infrared view with MIPS $24 \mu\text{m}$, *Herschel* $70 \mu\text{m}$, and $100 \mu\text{m}$. The PANIC images are shown for *H* and *Ks* bands because their image quality is better, while the *J*-band image is from ISPI. Very little emission is detected in the vicinity of IRS2 at wavelengths lower than $2.2 \mu\text{m}$, and the image is dominated by the scattered light nebula on the blueshifted side of the IRS1 outflow. The near-infrared images on larger scales detect the shocked- H_2 emission from both outflows (Bourke 2001). The *Spitzer* IRAC data show the scattered light emission from both IRS1 and IRS2 in addition to outflow knots more clearly, as shown previously by Chen et al. (2008). Then the MIPS $24 \mu\text{m}$ and *Herschel* PACS 70 and $100 \mu\text{m}$ data detect the thermal mid- to far-infrared emission from the inner envelopes of both protostars. IRS2 is clearly resolved from IRS1 and also appears much redder than IRS1 with substantially lower $24 \mu\text{m}$

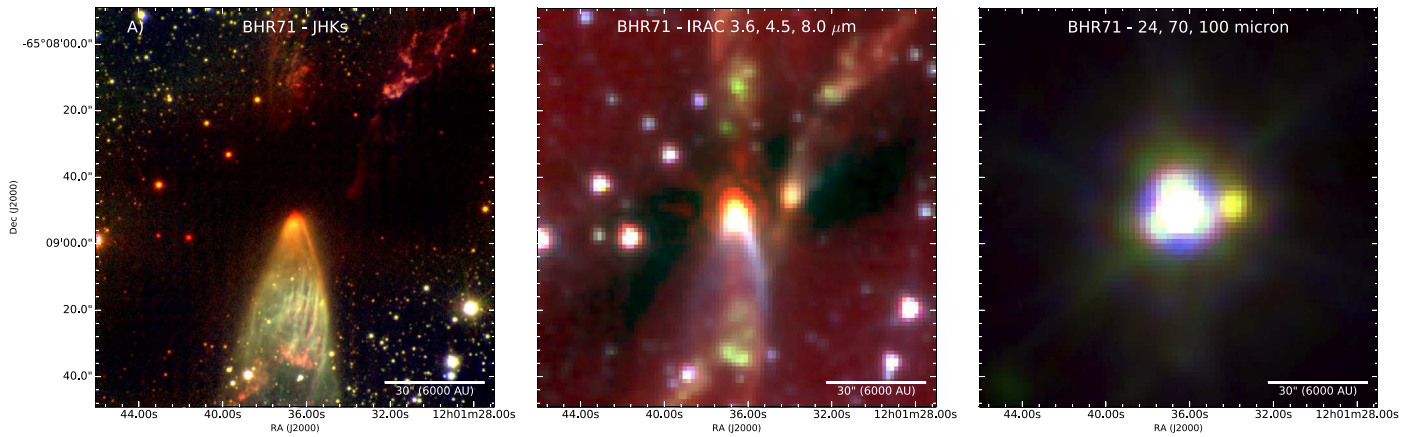


Figure 1. False-color images of BHR71 at multiple wavelengths. The left panel shows BHR71 as viewed in the near-infrared in Ks (PANIC), H (PANIC), and J bands (ISPI). The outflow cavity from the blueshifted outflow of IRS1 is quite prominent and the outflow cavity from IRS2 is not distinct, but several knots are apparent in the northwest portion of the image. The middle panel shows the *Spitzer* 3.6, 4.5, and 8.0 μm images on the same scale. IRS1 is still dominant, but IRS2 is much more apparent. The right panel shows the *Spitzer* 24 μm image along with *Herschel* 70 and 100 μm imaging that clearly resolves the mid- and far-infrared emission that is directly associated with both IRS1 and IRS2. IRS1 is quite prominent at all three wavelengths, but IRS2 is not strongly detected until 70 and 100 μm because of its deeply embedded nature. All images map the longest wavelength to red, the intermediate wavelength to green, and the shortest wavelength to blue.

emission. The PACS images were previously published by Yang et al. (2017).

We show a larger field of view around BHR71 from *Spitzer* IRAC and *Herschel* SPIRE in Figure 2. The *Spitzer* IRAC data show the envelope surrounding BHR71 in extinction against the 8 μm Galactic background, in addition to the extended outflow knots from both sources. The SPIRE maps show the submillimeter emission from the extended BHR71 core surrounding IRS1 and IRS2, emitting where the 8 μm absorption is apparent. At wavelengths longer than 250 μm , IRS1 and IRS2 are no longer resolved. There is faint 500 μm emission (appearing red) along the direction of the IRS1 outflow. This may be the result of CO ($J = 5 \rightarrow 4$) emission contaminating the longest wavelength SPIRE band, similar to the known CO contamination to SCUBA-2 maps from the ($J = 3 \rightarrow 2$) and ($J = 6 \rightarrow 5$) lines (e.g., Drabek et al. 2012).

3.1. SED Class of IRS1 and IRS2

The broad wavelength coverage from the near-infrared to the submillimeter also enables us to more quantitatively characterize these two protostars. To accurately distinguish the observational class for both IRS1 and IRS2, we used PSF photometry from *Herschel* at 70, 100, 160, and 250 μm , aperture photometry between 3.6 μm and 24 μm and millimeter flux measurements from ALMA, ATCA, SEST, and SIMBA, see Table 2. All these data are used to construct the SEDs shown in Figure 3 for IRS1 and IRS2 individually, as well as the combined emission of the sources. The bolometric luminosity for BHR71 as a whole is $17.7 L_{\odot}$. The more luminous source, IRS1, has $L_{\text{bol}} = 14.7 L_{\odot}$ and a bolometric temperature ($T_{\text{bol}} = 68$ K), while the fainter source IRS2 has $L_{\text{bol}} = 1.7 L_{\odot}$ and $T_{\text{bol}} = 38$ K. Thus, while IRS1 is about ten times more luminous, both are Class 0 protostars, with IRS2 possibly being slightly less evolved. The relative inclinations of IRS1 and IRS2 could contribute to their observed T_{bol} difference, but they are both moderately inclined with respect to the line of sight (see Section 3.3), and it is difficult to determine if this would fully account for the observed difference. We calculate L_{bol} by integrating the SED using the trapezoidal integration method implemented in the IDL function *tsum*. Then, T_{bol} is calculated following Myers & Ladd (1993; also using *tsum*) in

the calculation of the average frequency of the SED. T_{bol} is the temperature of a blackbody with the same average frequency as the observed SED (Ladd et al. 1991; Chen et al. 1995; Myers et al. 1998).

3.2. ATCA and ALMA Continuum Data

Continuum emission is detected toward both BHR71 IRS1 and IRS2 at 1.3 mm and 1.3 cm with ALMA and ATCA, respectively, see Figure 4. The ALMA 1.3 mm emission is clearly detected toward both protostars, with IRS1 being ~ 12 times brighter at 1.3 mm than IRS2 (Table 2). There is also some extended emission away from the protostar positions, tracing the envelope, and some tenuous emission detected in between IRS1 and IRS2. The emission between IRS1 and IRS2 is possibly analogous to the continuum emission that apparently connects IRAS 16293-2422 A and B (Jacobsen et al. 2018). The well-resolved structure of IRS1 makes Gaussian fitting unreliable for this source. The major and minor axes of IRS1 out to the 3σ level are $\sim 9''$ and $\sim 7''$, respectively. IRS2, on the other hand, is more symmetric. The major and minor axes to the 3σ level are both $\sim 3''.9$, but Gaussian fitting yields a deconvolved major axis of $1''.69$ and a minor axis of $1''.23$ with a position angle of $87^\circ.5$. However, the source does not appear to be well resolved, and the source size from Gaussian fitting may not be overly accurate.

To measure the ALMA 1.3 mm continuum flux densities as reliably as possible, we generated a sigma-clipped map, where pixels below the 3σ level ($\sigma = 0.68$ mJy) are set to zero to avoid including excess noise in the measurement of the flux density. This method will, however, exclude a small amount of real emission, but will result in a more repeatable measurement of flux density. We measured the combined emission from IRS1 and IRS2 in a $35''$ diameter circle centered between the sources, finding a flux density of 1.41 ± 0.02 Jy. The flux density of IRS1 alone was measured within a $25''$ diameter circle centered on IRS1, measuring a flux density of 1.28 ± 0.01 Jy. Finally, the flux density for IRS2 was measured in a $10''$ diameter aperture, centered on IRS2, measuring a flux density of 0.12 ± 0.005 Jy. Note that the uncertainties on flux densities are only statistical.

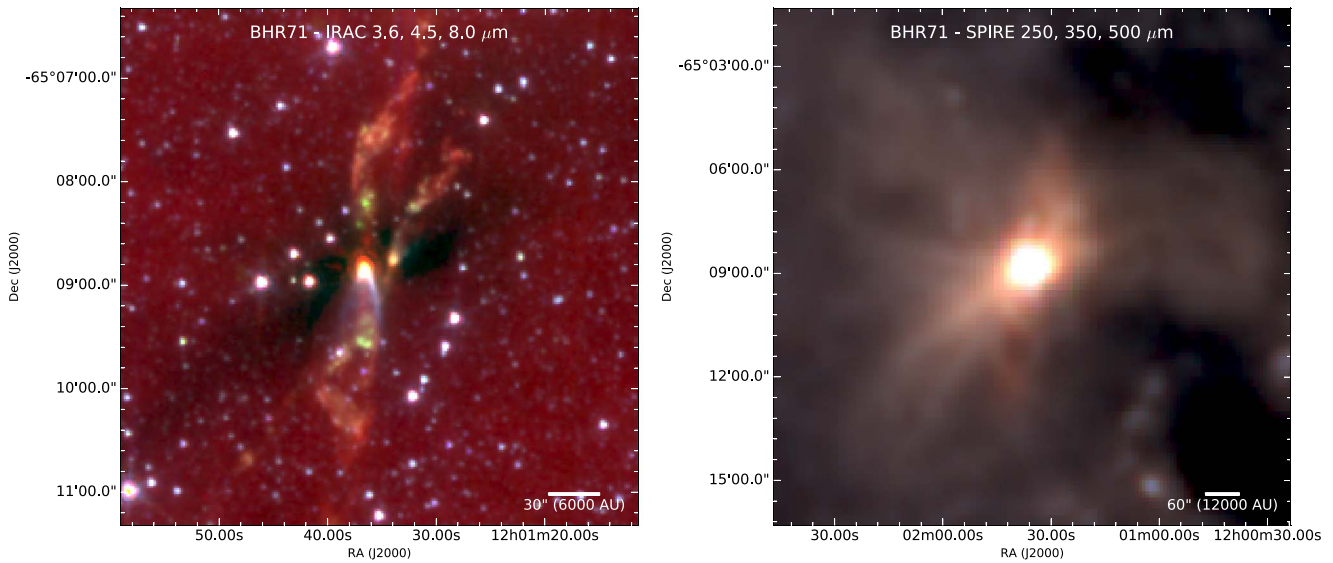


Figure 2. False-color images of BHR71 showing a larger-scale view from *Spitzer* at 3.6, 4.5, and 8.0 μm (left panel). The extended envelope is apparent in absorption against the 8.0 μm infrared background. The right panel shows the submillimeter view of BHR71 at 250, 350, and 500 μm covering a field of view twice as large as in the left image. The red feature at 500 μm in the outflow direction might be contamination from CO ($J = 5 \rightarrow 4$) emission. The core surrounding the protostars is quite extended and well resolved even at the longest wavelengths.

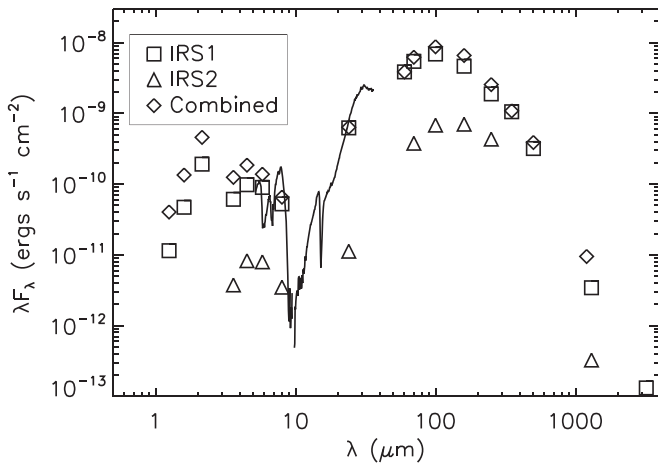


Figure 3. Spectral energy distribution from the near-infrared to the millimeter constructed from photometry presented in this work, as well as photometry and spectroscopy from the literature. From the SEDs, IRS1 and IRS2 are measured to have $L_{\text{bol}} = 14.7, 1.7 L_{\odot}$ and $T_{\text{bol}} = 68, 38$ K, respectively. The two protostars are well resolved shortward of 70 μm and at wavelengths where they can be observed with interferometry. The fluxes toward IRS1 and IRS2 are measured with PSF photometry between 70 to 250 μm . IRS1 is plotted with squares, IRS2 is plotted with triangles, and the combined SED is plotted with diamonds. IRS1 clearly dominates the SED, but IRS2 has a lower T_{bol} , and the SED is seen to peak at slightly longer wavelengths than IRS1 because of its more deeply embedded nature. The solid line is the *Spitzer* IRS spectrum from Yang et al. (2017).

The ATCA 1.3 cm continuum data also resolve IRS1 and IRS2, although IRS2 is much fainter; IRS2 is only detected at the 4σ level, 12.5 times fainter than IRS1. Since the sources appear point-like and not highly resolved, we measured the flux densities by simultaneously fitting Gaussians to each source using CASA. The measured flux densities for IRS1 and IRS2 are 2.7 and 0.22 mJy, respectively. Chen et al. (2008) also detected both IRS1 and IRS2 at 3 mm; thus, with the addition of our data, we can examine the radio spectrum toward IRS1 and IRS2, shown in Figure 5. The emission from both IRS1 and IRS2 is consistent with dust-only emission out to 1.3 cm,

but with a shallow spectral slope, 2.7 ± 0.2 for IRS1 and 2.9 ± 0.5 for IRS2 ($F_{\nu} \propto \lambda^{-\alpha}$). In this formalism, the expected spectral index for dust emission is $\alpha = (2 + \beta)$, where β is the dust opacity spectral index and $\beta \sim 1.8$ is expected for dust grains in the interstellar medium. Our data indicate β of 0.7–0.9, which is consistent with other studies of dust opacity in protostars (Kwon et al. 2009; Chiang et al. 2012). However, we cannot rule out some contribution from free-free emission from either protostar at 1.3 cm.

We can use the dust continuum data to estimate the inner envelope (and presumed disk) masses surrounding IRS1 and IRS2. We do this by assuming isothermal and optically thin dust emission, adopting the dust-only opacity at 1.3 mm from Ossenkopf & Henning (1994) with $\kappa_{1.3\text{mm}} 0.899 \text{ cm}^2 \text{ g}^{-1}$, and assuming a dust-to-gas mass ratio of 1:100 (Bohlin et al. 1978). We assume a dust temperature of 20 K for IRS1 and IRS2, comparable to the expected envelope temperatures at ~ 1000 au scales for the luminosities of IRS1 and IRS2 (Whitney et al. 2003). Finally, employing the equation

$$M_{\text{dust}} = \frac{D^2 F_{\lambda}}{\kappa_{\lambda} B_{\lambda}(T_{\text{dust}})}, \quad (1)$$

we estimate a total mass (dust+gas) for the inner envelopes/disks of both IRS1 and IRS2 of $1.25 M_{\odot}$ from the measured flux density of 1.41 Jy. The flux densities for IRS1 and IRS2 are 1.28 Jy and 0.12 Jy, respectively, leading to respective dust+gas masses of 1.13 and 0.11 M_{\odot} if the same temperature is assumed for both sources. Since IRS1 is a factor of ~ 8.6 more luminous than IRS2, its average dust temperature should be a factor of ~ 1.7 higher (34 K) than that of IRS2, assuming that $T \propto L^{0.25}$. With an assumed dust temperature of 34 K for IRS1, the estimated mass becomes 0.59 M_{\odot} , making the combined mass 0.7 M_{\odot} considering the likely higher temperature for IRS1.

These masses are for the inner envelope and disk around the protostars, the larger-scale envelope traced by *Herschel* (Figure 2) is resolved out and not detected in the ALMA

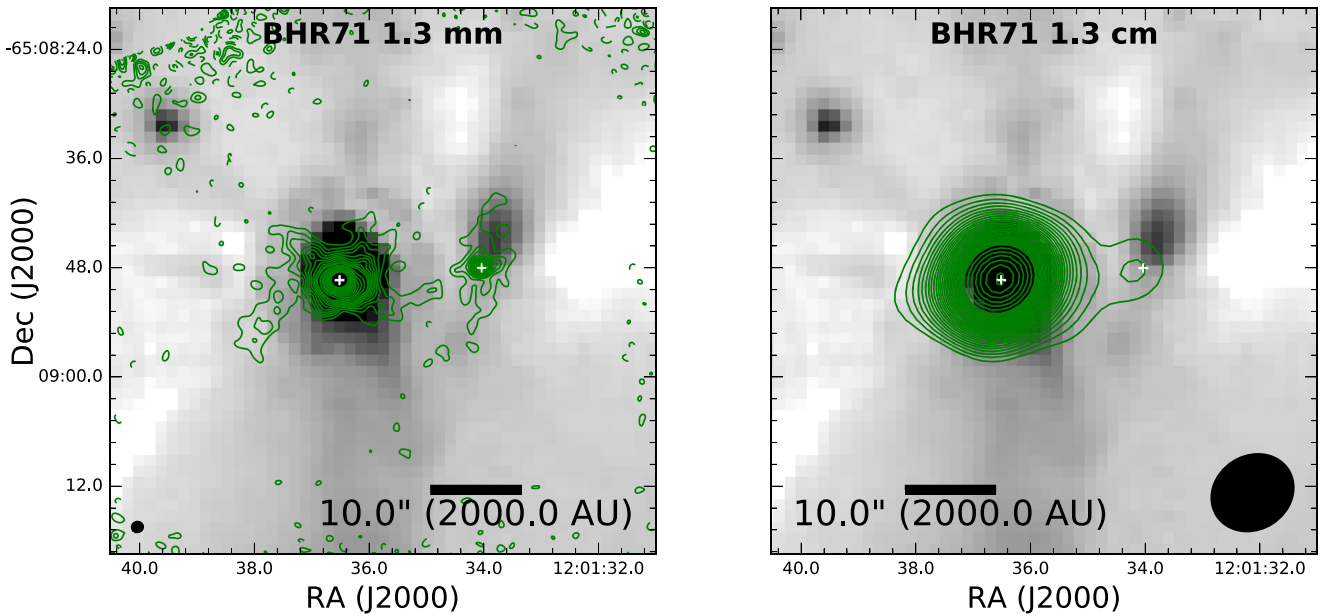


Figure 4. ALMA 1.3 mm and ATCA 1.3 cm contours overlaid on the *Spitzer* 8 μ m image (grayscale) are shown in the left and right panels, respectively. The ALMA image at higher resolution shows the dust emission corresponding to the location of the brightest 8 μ m emission toward BHR71 IRS1, but toward IRS2, the 1.3 mm emission is located at the base of the 8 μ m emission. The same behavior is also shown by the ATCA 1.3 cm image. The ATCA image might be tracing a combination of both free-free and dust emission. The ALMA 1.3 mm emission shows extended features; IRS1 shows features extended apparently along the outflow cavity walls, and there is an extension of emission from IRS1 toward the location of IRS2. The contours in both panels start at 3σ and increase in 3σ intervals, where $\sigma_{1.3\text{mm}} = 0.5 \text{ mJy beam}^{-1}$ and $\sigma_{1.3\text{cm}} = 0.1 \text{ mJy beam}^{-1}$.

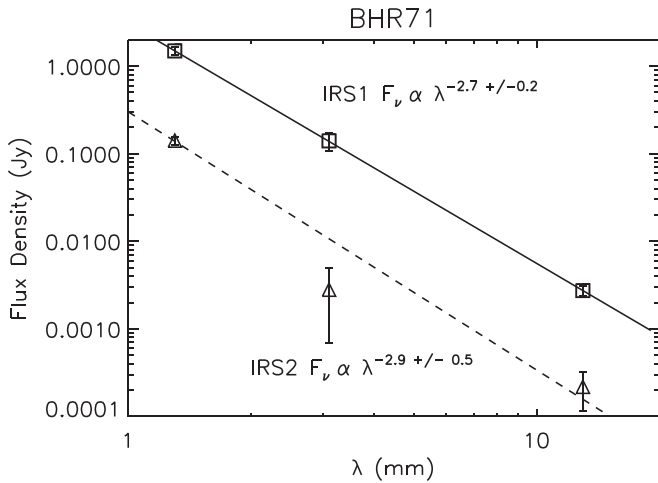


Figure 5. Millimeter to centimeter spectra of BHR71 IRS1 and IRS2. The two spectra are compatible with dust emission down to 1.3 cm, but we cannot rule out a contribution of free-free emission at 1.3 cm toward both protostars. The 3.1 mm data point toward IRS2 seems quite low compared to the others, given that it would indicate an unphysically steep spectral slope, but this is also the data point with the lowest S/N.

observations. Thus, these mass estimates should be considered lower limits.

The continuum and photometric data enable us to classify the two protostars and measure the amount of mass surrounding the protostars; however, these data do not specifically reveal what led to the formation of the binary system other than there being a large mass reservoir in the envelope surrounding BHR71. To better characterize the formation of the binary system, we must turn to the molecular line data to trace the kinematics of the gas surrounding the protostars. First we briefly examine the outflows of BHR71 observed by ALMA, however.

3.3. Outflow Morphology from ALMA

The outflows from BHR71 IRS1 and IRS2 are quite prominent in the scattered light images from the near-infrared and *Spitzer*. However, we also traced the outflow with ^{12}CO and ^{13}CO observations with ALMA (Figure 6). The integrated intensity maps of the CO emission from IRS1 and IRS2 (Figure 6) clearly show the red- and blueshifted sides of both outflows. The ^{12}CO maps indicate that the outflows of the two protostars are inclined in opposite directions. The blueshifted side of the outflow from IRS1 is on the south and the redshifted side is to the north, while this is opposite in the case of IRS2. This orientation of the outflows has previously been indicated in the near-infrared and IRAC imaging as well as in single-dish observations (Bourke 2001; Parise et al. 2006). We also find that C^{18}O traces the edge of the outflow cavity walls toward IRS1 in Figure 6. From these data, we measure outflow position angles of 174° and -31° for IRS1 and IRS2, respectively. The angles are measured east of north and are found by drawing a line that bisects the outflow cavity and passes through the continuum position.

The outflow from IRS2 has a more narrow opening angle than the outflow of IRS1. The outflow opening angles of IRS1 and IRS2 are 55° and $\sim 47^\circ$, respectively, measured at a distance of $10''$ from the protostars. Note that these are the full opening angles of the outflow cavities. Radiative transfer modeling studies typically quote the half-opening angles (Whitney et al. 2003). The ^{13}CO emission from IRS1 traces lower-velocity emission better than ^{12}CO , and we measure a slightly larger opening angle of $\sim 63^\circ$. The outflow from IRS2 is not well detected in ^{13}CO , and we are unable to make a similar measurement.

The redshifted side of the outflow toward IRS2 shows peculiar structure at distances greater than $10''$ from the protostar. Along the line of sight, the blueshifted outflow of IRS1 and the redshifted outflow of IRS2 overlap. The northern

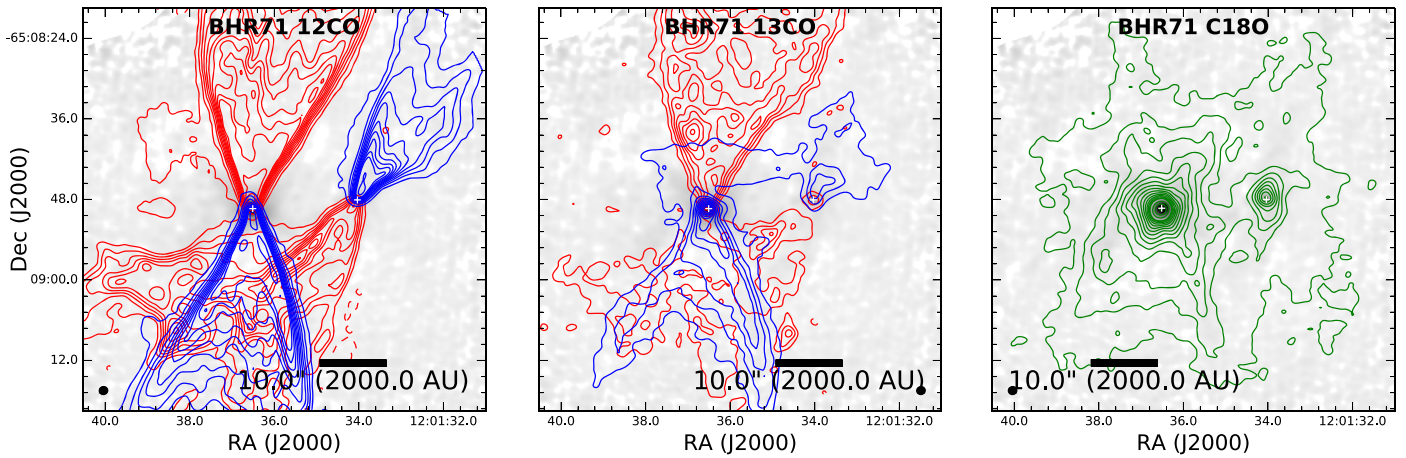


Figure 6. Integrated intensity maps of ^{12}CO , ^{13}CO , and C^{18}O ($J = 2 \rightarrow 1$) overlaid on the ALMA 1.3 mm continuum image (grayscale). ^{12}CO and ^{13}CO are divided into red- and blueshifted components, with corresponding contour colors; C^{18}O includes both the blue and red components. ^{12}CO and ^{13}CO clearly show the outflow emission from the protostars in both lines, with the redshifted lobe of the IRS2 outflow being quite broad. The outflow cavities are clearly not axisymmetric, but the IRS1 cavity especially appears to show reflection symmetry. The C^{18}O is peaked toward both protostars, tracing the warm inner envelopes. The ^{12}CO is integrated between -15 to -5.6 km s^{-1} and -3 to 4 km s^{-1} , and $\sigma_{\text{blue,red}} = 0.46, 0.4$ K km s^{-1} , respectively. The blue and red contours start at 20σ and increase in this same interval. ^{13}CO is integrated between -7 to -4.7 km s^{-1} and -3.2 to -1.5 km s^{-1} , and $\sigma_{\text{blue,red}} = 0.13, 0.15$ K km s^{-1} , respectively, with the blue contours starting at 50σ and increasing in 20σ intervals, while the red contours start 20σ and increase in this same interval. C^{18}O is integrated between -5.8 to -3.2 km s^{-1} , and $\sigma = 0.13$ K km s^{-1} and the contours start at 15σ and increase in 10σ intervals.

side of the redshifted outflow from IRS2 fans out to a much larger opening angle at this point, and this continues past the point where the outflow cavities overlap. This wider feature also appears in the ^{13}CO integrated intensity map at lower S/N.

A more in-depth study of the outflow system will be presented by T. Bourke et al. (2018, in preparation). However, we can make some estimates of the source inclinations using the outflow geometry in the absence of detailed modeling. This is possible because there is very limited overlap between the blue- and redshifted sides of both outflows. Assuming that the outflows are conical, the lack of significant overlap of blue- and redshifted sides, both along the outflow and toward the protostars, means that the IRS1 outflow must have an inclination between 35° and 63° , because its opening angle is $\sim 55^\circ$. The outflow is likely closer to 63° than the other extreme because of how extended it is in the plane of the sky. The IRS2 outflow with a more narrow opening angle of $\sim 47^\circ$ must have an inclination between 43° and 67° . We define 90° as viewing the system edge-on, where the outflow is entirely in the plane of the sky, and 0° is edge-on, where the outflow is completely along the line of sight.

4. Dense Molecular Line Kinematics

The data sets from Parkes, ATCA, and ALMA (Table 1) combined trace the kinematics of the dense gas from the scale of the entire BHR71 core to the envelopes surrounding the individual protostars. It is instructive to start from the largest scales and move inward, thus we begin with a discussion of the Parkes data. To introduce the data, we show the spectrum of each line toward each source (both sources for Parkes) and plot them in Figure 7. The spectra are extracted from a circular region matching the size of the beam in each observation (see Table 1), except for the ALMA data, where we extract the spectra within a circle with a diameter of $5''$. ^{12}CO and ^{13}CO have broad line widths tracing the outflow, and C^{18}O mainly traces the inner envelope with some outflow contamination. N_2D^+ traces the cold envelope, and this molecule is mostly destroyed in the $5''$ region around IRS1, and NH_3 also traces

the cold gas, but on the larger scales probed by ATCA. Given that NH_3 and N_2D^+ have lower intensities at the protostar positions, we also extracted spectra from the position of the N_2D^+ emission peaks east of IRS1 and east of IRS2. These positions show the hyperfine structure of N_2D^+ and NH_3 better.

The largely distinct regions traced by CO and its isotopologues and NH_3 , N_2D^+ , and N_2H^+ are the result of both the thermal structure of the infalling envelopes and chemical processes. CO is frozen out onto dust grains at temperatures below ~ 20 K and at typical densities of star-forming cores $n > 10^5$ cm^{-3} (Frerking et al. 1982; Benson & Myers 1989). Observations and astrochemical models show that N_2H^+ , N_2D^+ , and NH_3 form abundantly in these cold, dense regions where CO is frozen out (e.g., Bergin et al. 2002; Caselli et al. 2002; Lee et al. 2004). However, in the central regions of the protostellar envelopes, the temperature increases due to heating from the protostar and accretion, which evaporates CO from the dust grains inside $R \sim 1000$ au (the actual radius depends on the luminosity). In this region, the reaction of CO with N_2H^+ and N_2D^+ is extremely efficient and rapidly destroys these molecules. Moreover, N_2D^+ formation is shut off at $T \sim 20$ K because the key molecule in its formation pathway, H_2D^+ , is converted back into H_3^+ and HD (e.g., Herbst 1982). Then there is also a destruction pathway for NH_3 involving reactions with HCO^+ , which will form in the presence of CO (Lee et al. 2004); there is also the possibility that NH_3 will freeze out onto dust grains before it is completely destroyed by HCO^+ at $n > 10^6$ cm^{-3} (Visser et al. 2011). This leads to the onion-like chemical structure of protostellar envelopes where N_2H^+ , N_2D^+ , and NH_3 exist in gas phase in the outer regions, not in the inner regions, and CO exists most prevalently in the inner regions without N_2H^+ , N_2D^+ , and NH_3 . We note, however, that these are not the only molecules in the gas phase in these regions.

4.1. Parkes NH_3 Kinematics

The Parkes data traced the NH_3 (1, 1) emission line with $60''$ (12,000 au) resolution out to $8'$ (~ 0.5 pc) scales, probing the

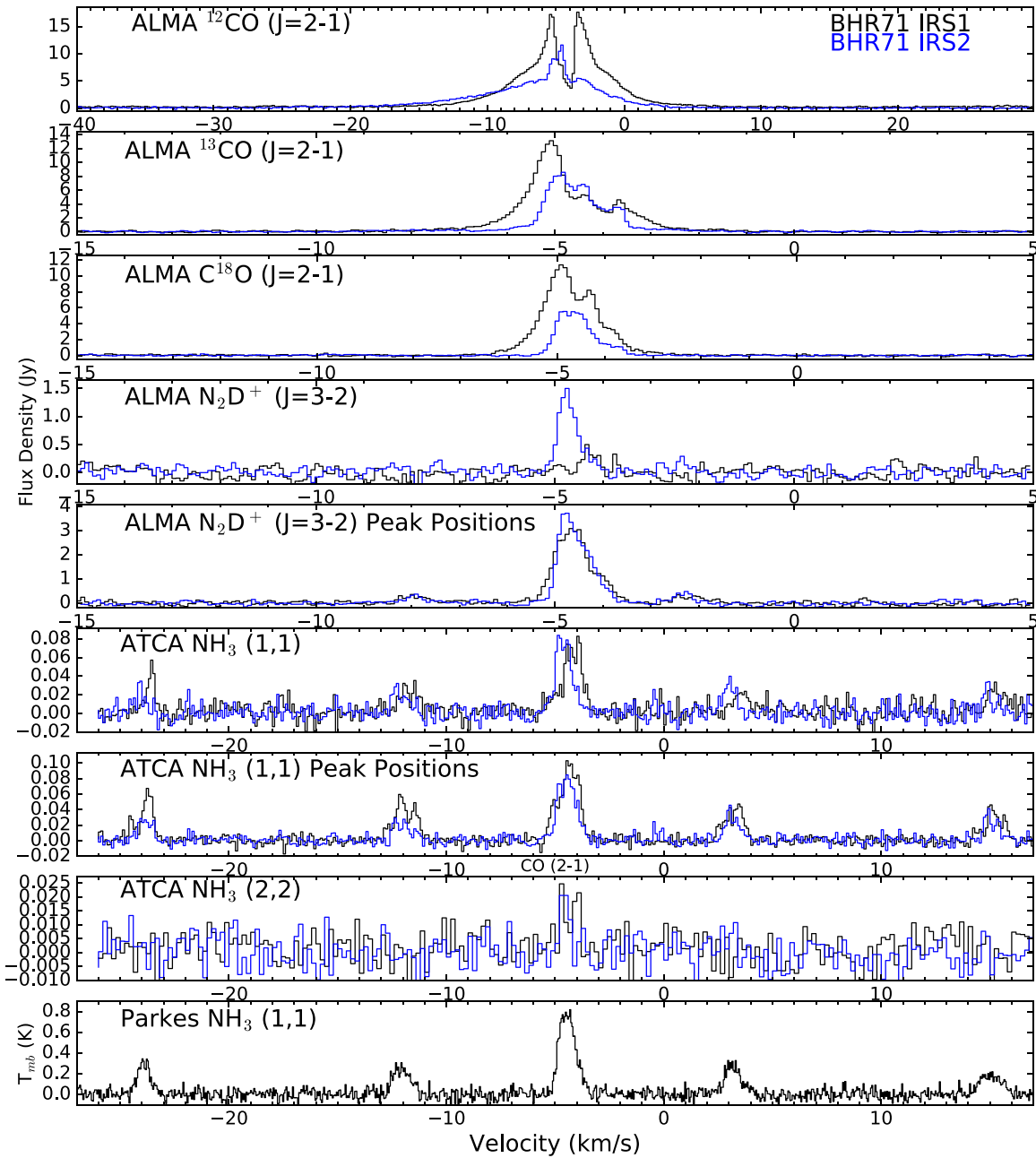


Figure 7. Spectra toward the positions of BHR71 IRS1 and IRS2 for each observed molecule. The ALMA spectra are extracted from a $5''$ circle centered on the protostars, the ATCA spectra are extracted from a circle matching the synthesized beam ($\sim 10''$) centered on the protostars, and the Parkes spectrum is extracted from a $60''$ circle centered on IRS1. ALMA and ATCA N_2H^+ and N_2D^+ spectra are also extracted from the emission peaks closest to IRS1 and IRS2 in the panels containing the text “Peak Positions.” Some spectra are shown in different velocity ranges to highlight different features of the spectra.

largest scales available to us in molecular gas. NH_3 emission is detected from the entire region where the envelope is seen in absorption at $8\ \mu\text{m}$ (Figure 2), and extending slightly beyond the edge of the map to the southeast, as shown in Figure 8. The emission probably does not extend beyond the northern end of the map; the intensity appears to rise here due to increased noise at the map edge.

Using the NH_3 fitting routines in CLASS, we fit the hyperfine lines in each pixel of the map where emission was detected above the 5σ level and the line-center velocity and line-width maps that are also shown in Figure 8. The line-center velocity map shows a slight velocity gradient along the long axis of the NH_3 emission from southeast to northwest, in the same direction as the extended $8\ \mu\text{m}$ extinction. The total

velocity change is about $0.15\text{--}0.2\ \text{km s}^{-1}$, corresponding to a gradient of about $1\ \text{km s}^{-1}\text{pc}^{-1}$. We measure the velocity gradient more quantitatively by fitting the slope of a 1D cut along the envelope orthogonal to the outflow of IRS1 and by fitting a 2D plane to the line-center velocity maps. The resulting velocity gradient orthogonal to the outflow direction is $1.2\ \text{km s}^{-1}\text{pc}^{-1}$ and the 2D velocity gradient fit finds a gradient of $1.15\ \text{km s}^{-1}\text{pc}^{-1}$ with a position angle of 101° east of north. This velocity gradient could be interpreted as core rotation, as is often done (e.g., Goodman et al. 1993), but it was shown in Tobin et al. (2011, 2012b) that infalling flows along asymmetric envelopes could also produce velocity gradients. If the velocity gradient of the core reflects rotation, then IRS2 should orbit around IRS1 in the same direction as the core

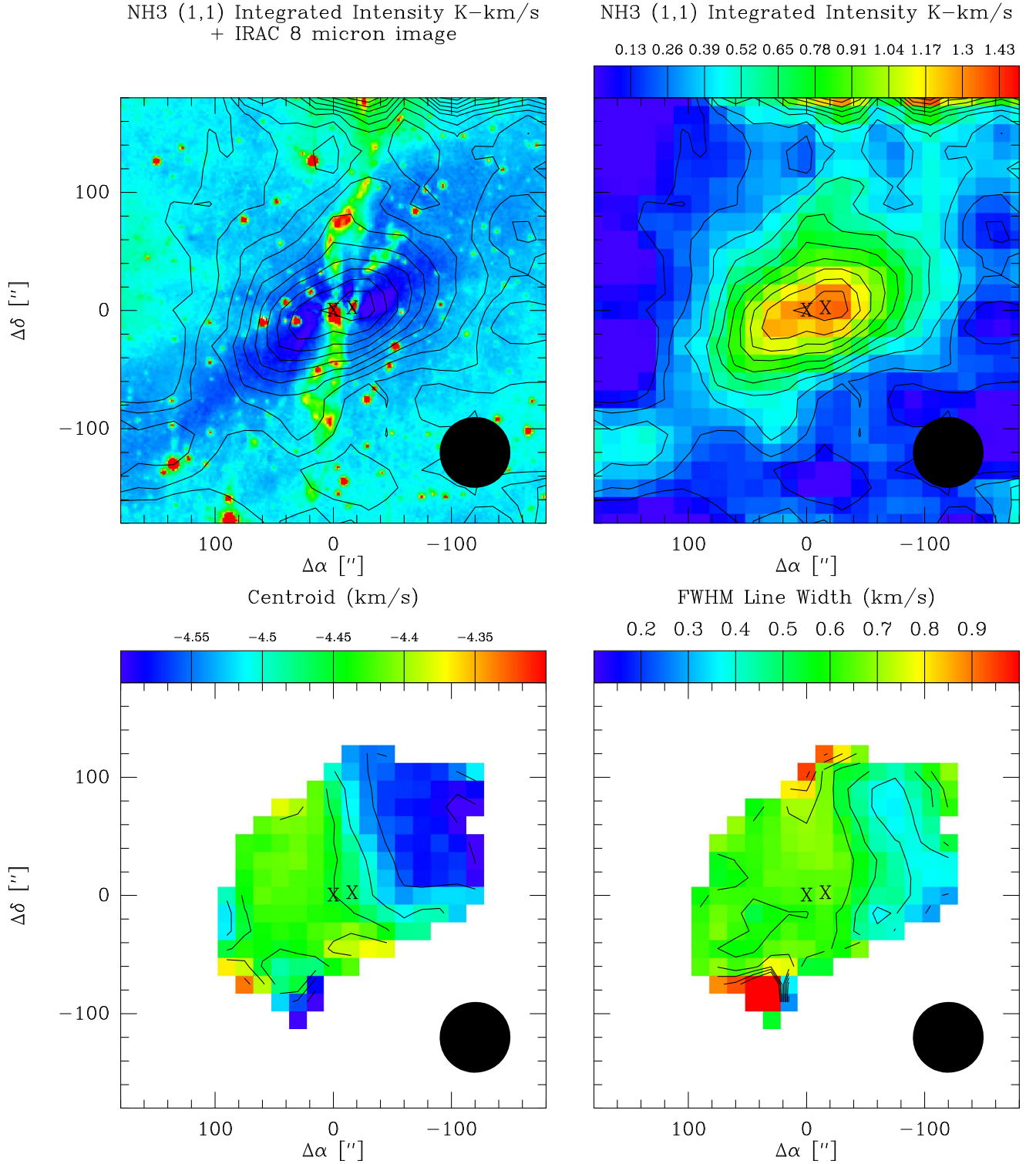


Figure 8. Parkes single-dish NH_3 (1, 1) maps. The upper left panel shows the integrated intensity of the main NH_3 (1, 1) hyperfine lines overlaid on the *Spitzer* 8 μm image (color scale). The upper right panel shows just the integrated intensity of the main NH_3 (1, 1) hyperfine lines (color scale and contours). The lower left panel shows the line-center velocity derived from a fit to all the NH_3 (1, 1) hyperfine lines, and the lower right panel shows the line width also derived from fitting all hyperfine components. The integrated intensity peaks toward the position of IRS2, and the velocity map shows a very small gradient across the source, only about a 0.15 km s^{-1} differential. The line-width map shows that the lines are narrow, at most only about 0.6 km s^{-1} wide. The positions of the IRS1 and IRS2 are marked with crosses. The intensity levels in the top panels are from the integrated intensity map of the main hyperfine lines between -6.5 to -2.2 km s^{-1} ; the intensity levels start at and increase in 3σ intervals, where $\sigma = 0.045 \text{ K km s}^{-1}$.

rotation. Furthermore, if IRS1 and IRS2 fragmented within this rotating core, the individual envelopes should have rotation in the same direction in the case of angular momentum conservation.

The line-width map in Figure 8 shows some variation across the source. The southern-most tip of the map has a very broad line width; this appears real and could be in an area affected by the two outflows. The eastern side of the line-width map is

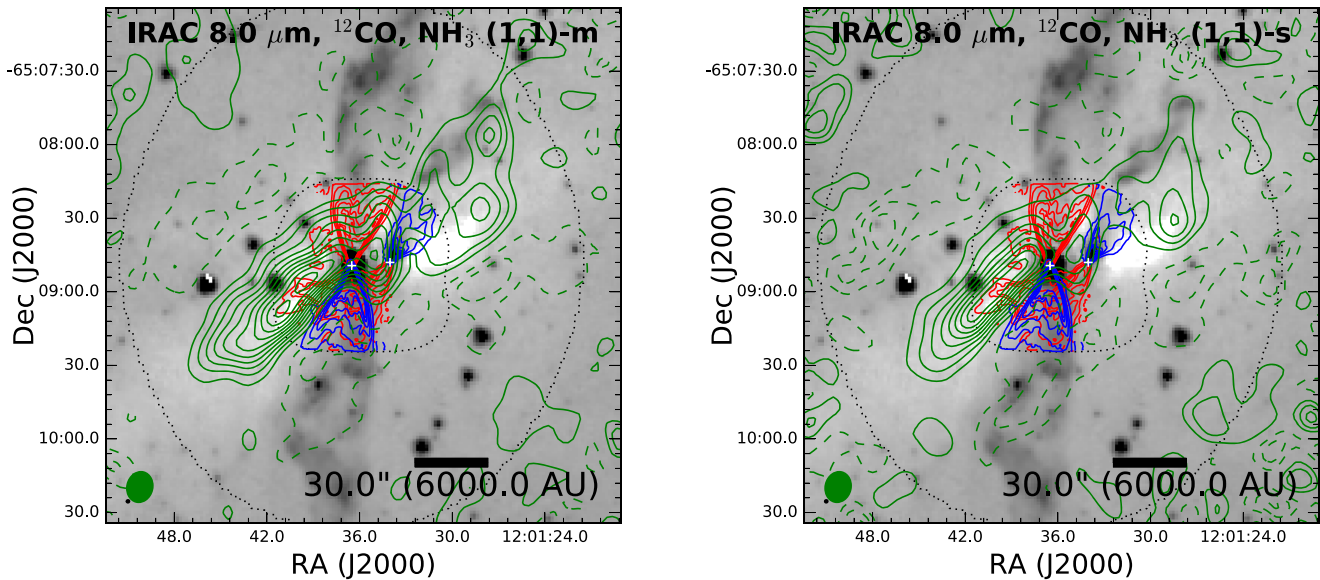


Figure 9. Integrated intensity contours from the ATCA NH_3 (1, 1) observations (green) overlaid on the *Spitzer* $8\ \mu\text{m}$ image (inverse grayscale). The integrated intensity of the main NH_3 lines is shown in the left panel and the satellite lines are presented in the right panel (between -12.6 to $-11.4\ \text{km s}^{-1}$). We also overlay the ^{12}CO red- and blueshifted integrated intensity contours (with corresponding colors) from Figure 6, showing the relationship of the outflow with the dense gas. The NH_3 (1, 1) emission at this higher resolution shows excellent correspondence with the $8\ \mu\text{m}$ absorption feature of the envelope on the background, and the NH_3 maps exhibit a cavity and depressions toward the location of IRS1. IRS2 is located directly beside an NH_3 peak. The NH_3 main and (satellite) contours start at 5σ (3σ) and increase in 5σ (3σ) intervals, where $\sigma = 0.075\ \text{K km s}^{-1}$ ($0.072\ \text{K km s}^{-1}$). A -5σ (-3σ) contour is also drawn.

relatively constant at 0.5 to $0.6\ \text{km s}^{-1}$, and on the western side, the line width dips down to $\sim 0.3\ \text{km s}^{-1}$. These line widths are in excess of the expected line width of NH_3 at $20\ \text{K}$ of $0.13\ \text{km s}^{-1}$, indicative of an additional nonthermal component. Some part of this nonthermal component could come from unresolved velocity gradients in the envelope within the $60''$ beam.

While the Parkes data are quite informative of the large-scale velocity structure, they also demonstrate a clear need to follow the kinematics to smaller scales with interferometric data to fully characterize the formation pathway of IRS1 and IRS2.

4.2. ATCA NH_3 Kinematics

The ATCA observations detected significant NH_3 emission near the protostar, as shown in Figures 9 and 10. The emission morphology is quite filamentary, also concentrated along the extended envelope seen in extinction at $8\ \mu\text{m}$. The strongest emission is found southeast of IRS1 with another sub-peak located east of IRS2, between the sources. The emission west of IRS2 is more diffuse with lower surface brightness. We also note that the NH_3 emission does not peak at the locations of the protostars themselves, and the morphology of the emission from the main NH_3 lines is quite similar to that of the satellite lines. We overlay the ^{12}CO integrated intensity maps in Figure 9 to highlight the regions that the outflows may influence. At first glance, it does not appear likely that the NH_3 emission east and west of IRS1 is significantly affected by the outflows.

The kinematic structure derived from the ATCA observations (Figure 10) was also fit using the NH_3 fitting routines within CLASS. This was done for each pixel of the map where emission was detected above 5σ , see the Appendix. The ATCA kinematic structure bears some similarity to the Parkes observations, but shows some significant departures as well. The line-center velocity map has features that extend to both more redshifted and blueshifted velocities than were evident in

the Parkes map. North of IRS1, there is a redshifted feature with velocities greater than $-4.2\ \text{km s}^{-1}$, and there is a redshifted feature directly southeast of IRS1. These features may reflect outflow interaction with the envelope, as evidenced by the conical shape of the redshifted feature north of IRS1 and the position of the redshifted southeast feature along the edge of the NH_3 emission, bordering the cavity wall of the southern outflow lobe. The line-width map also shows a broad line width south of IRS1 and to the southeast; however, the line width is very narrow to the north of IRS1. Outflow interactions can produce an increased line width and/or changes in the line-center velocity.

Between IRS1 and IRS2 is a steep velocity gradient from redshifted to blueshifted in the line-center map that continues past the position of IRS2. The region with the steep velocity gradient shows an accompanying increase in the line-width map that results from the velocity gradient being unresolved; such a feature showed up several times for other sources in Tobin et al. (2011). This gradient from red to blue is in the same direction as the large-scale gradient observed in the Parkes NH_3 map. Beyond $\sim \pm 40''$ from IRS1 in the direction of the extended envelope, the line-center velocities are about equal in the southeast and northwest sides of the envelope. The line width northwest of IRS2 is narrow, between 0.2 and $0.3\ \text{km s}^{-1}$. To the southeast, the line width remains above $0.3\ \text{km s}^{-1}$ and may be the result of outflow-envelope interaction, as suggested before. However, the increased line-width feature extends beyond the edge of the outflow cavity, but there is an unknown 3D structure along the line of sight. Depending on the configuration of the material, the outflow could affect a larger area beyond its boundaries, and increased line width propagates into the envelope. Alternatively, if the envelope is filamentary and curved along the line of sight, gas falling in toward the protostar could yield an increased line width. To the west of IRS2, the line width is quite narrow, except for one area that has a line width of $0.5\ \text{km s}^{-1}$.

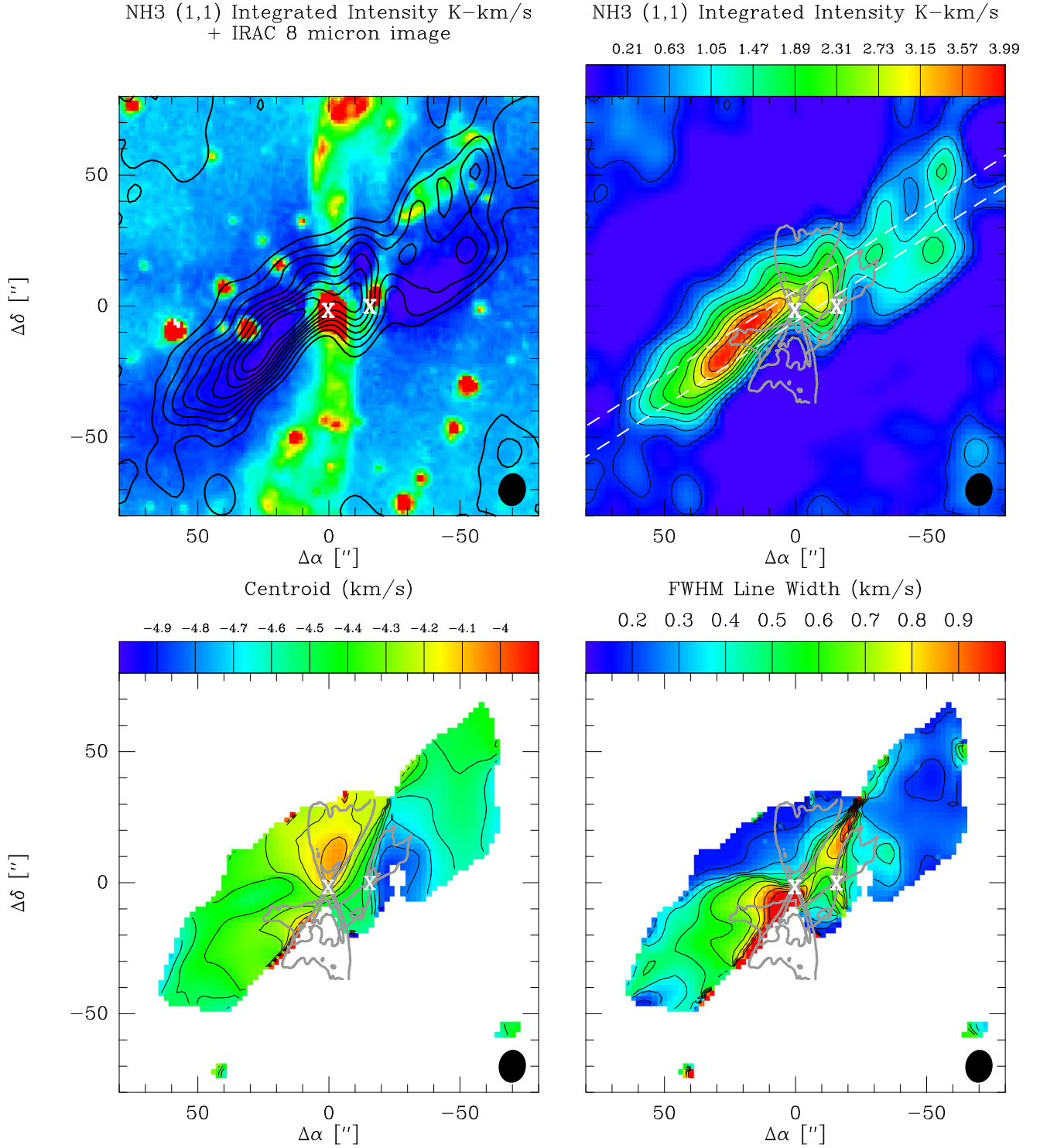


Figure 10. Same as for Figure 8, but for the ATCA NH_3 observations. The spatial extents of the outflows probed by ALMA in ^{12}CO are marked with the gray contours in all panels except in the top left panel. The velocity map shows considerably more structure than the Parkes map. The redshifted component appears to reflect the redshifted outflow cavity of IRS1, then there is an abrupt velocity gradient between IRS1 and IRS2. Some part of the velocity gradient is likely related to the outflow influence, but even without the additional velocity structure of the outflow, the gradient is quite strong. Furthermore, the gradient also appears as a region of large line width, which is caused by the change in line velocity on the scale of one beam width. There is also some evidence of outflow influence on the south side: the line width is increased where the eastern edge of the IRS1 outflow cavity is located, in addition to the redshifted side of the IRS2 outflow. However, the line width is not increased toward the redshifted side of the outflow where there appears to be a shift in the line-center map. The intensity levels in the top panels are from the integrated intensity map of the main hyperfine lines between -5.0 to -3.5 km s^{-1} ; the intensity levels start at 3σ and increase in 6σ intervals, where $\sigma = 0.07$ K km s^{-1} . The dashed lines in the upper right panel mark the region of position-velocity extraction.

We zoom-in on the immediate region around IRS1 and IRS2, the inner $60''$ of the source, in Figure 11, showing the line-center velocity in greater detail. From east to west,

crossing the source, the velocity changes from -4.55 km s^{-1} in the easternmost part of the map to -4.25 km s^{-1} at IRS1, -4.6 km s^{-1} at IRS2, and down to -4.85 km s^{-1} west of

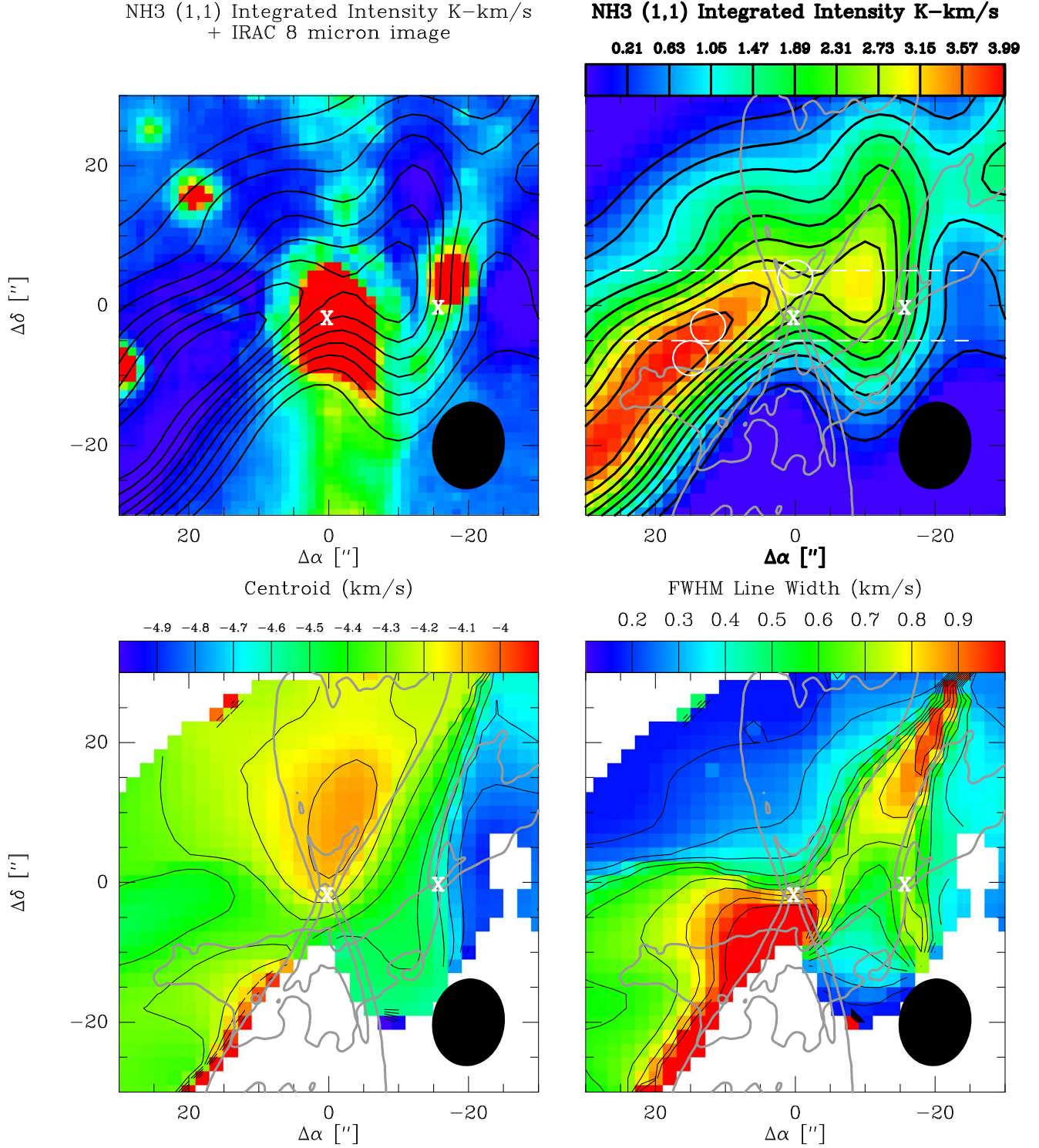


Figure 11. Same as Figure 10, but zoomed-in. The dashed circles in the upper right panel correspond to regions of spectral extraction to examine the quality of the hyperfine fitting, see the [Appendix](#)

IRS2. Qualitatively, the gradient changes from blue to red, and back to blue; thus, there is no clear velocity gradient that can be attributed to rotation around IRS1 and IRS2. Furthermore, the strip of broad line width directly north of IRS2 can be indicative of a rapid velocity change that can result from two velocity components along the line of sight. This was observed toward several protostars in Tobin et al. (2011), and the higher-resolution ALMA N_2D^+ data will be used to investigate this further.

The velocity profiles from the ATCA and Parkes velocity maps are extracted along lines orthogonal to the outflow directions and shown in Figure 12. The Parkes data show a velocity gradient comparable to the 2D fit. The ATCA profile shows significant structure near the protostar, and then the velocities return toward agreement with the cloud for IRS1. For IRS2, a very steep velocity gradient is derived from the ATCA data. The fits to the Parkes velocity gradients also find that the core velocity at the position of IRS1 is -4.45 km s^{-1} .

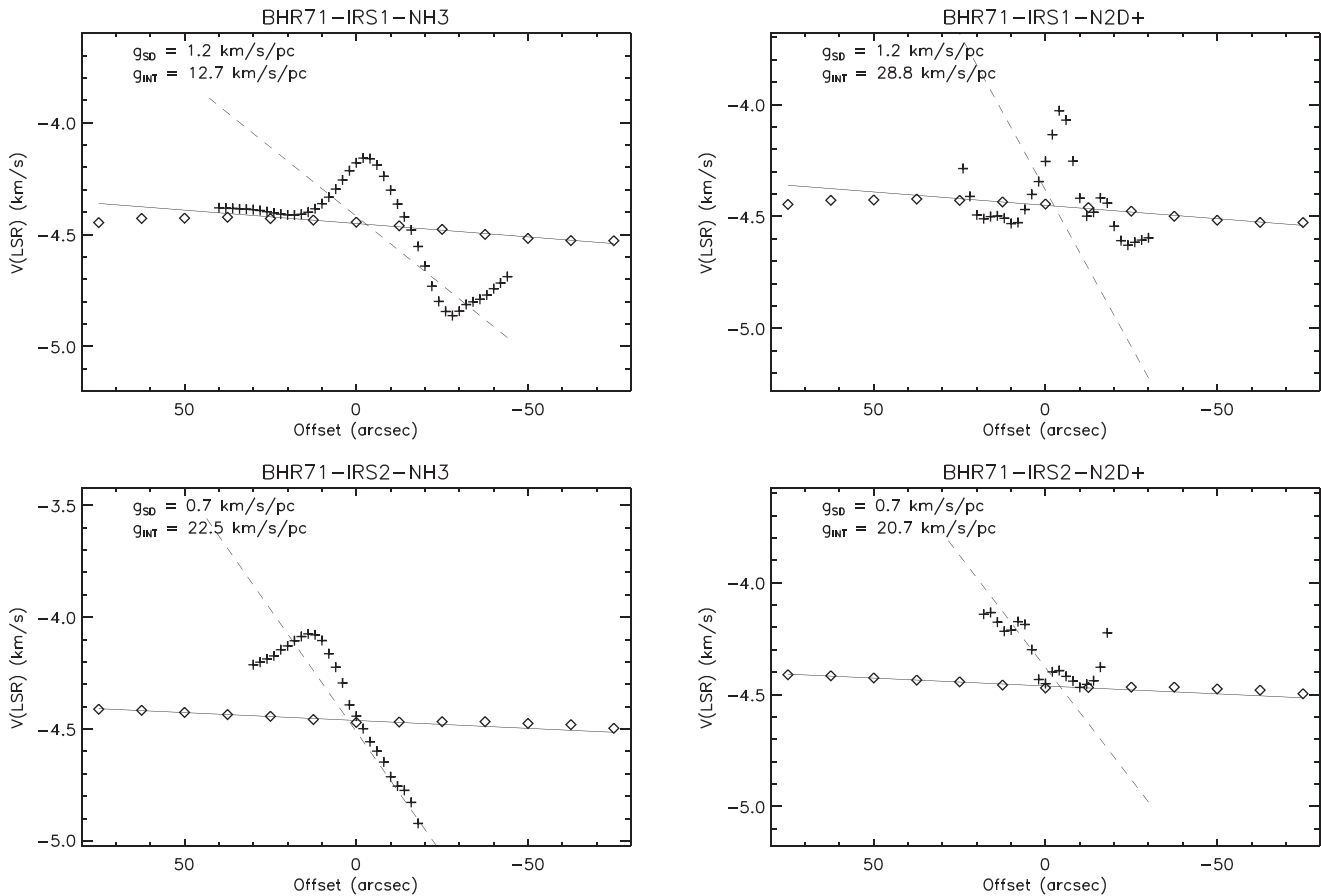


Figure 12. Velocity profiles extracted orthogonal to the outflow directions for IRS1 (top row) and IRS2 (bottom row). Velocity profiles are shown for both NH_3 (1, 1) (left panels) and N_2D^+ (right panels). All panels also show the profile extracted from the Parkes NH_3 data (diamonds), which is fit with a solid line. The single-dish data show a gradual velocity gradient and the interferometer data (pluses) show more structure. The N_2D^+ data may have different centroid velocities relative to that of NH_3 . The reason might be that N_2D^+ traces a different region of the cloud due to chemistry. The velocity gradients in the interferometer data are fit (dashed lines), but their structure limits the utility of the derived values.

The velocity and line-width maps derived from hyperfine fitting and the extracted profiles are useful for providing a global view of the envelope kinematics. However, the velocity and line-width maps can dilute some more detailed information provided by the line profiles. We show position–velocity (PV) diagrams for both the main NH_3 lines and satellite lines in Figure 14. These are extracted from a $10''$ strip in the east–west direction (position angle = 90°), centered on IRS1. PV diagrams extracted from NH_3 (1, 1) datacubes are complex because each hyperfine component is a pair of closely spaced lines, so caution must be exercised in their interpretation. Figure 14 shows that the western portion of the envelope (containing IRS2) is best described by a single-velocity component (-4.6 km s^{-1} and offsets between $-25''$ to $-5''$), and this component shows a slight gradient to more blueshifted velocities. However, another distinct velocity component is present on the east side of the envelope (-4.0 km s^{-1} and offsets between $-5''$ to $25''$), redshifted with respect to the far west side of the envelope. This is most evident in the PV diagram of the satellite lines where there appear to be three peaks; each velocity component of NH_3 has two hyperfine lines, and the velocity shift is strong enough for one hyperfine line from the blue and red component to overlap. This strong shift appears in the velocity map as the redshifted component that is coincident with the redshifted outflow from IRS1, but this redshifted component extends beyond the bounds of the

outflow. This could indicate that there is a second velocity component to the core, or that the outflow imparts a bulk redshifted velocity to the dense molecular gas in the envelope.

In addition to the PV diagrams in the equatorial cuts, we also show a PV diagram extracted from a larger region along the long axis of the envelope (a position angle of 123°) in Figure 13. This PV diagram shows that the features observed in the smaller region are present throughout much of the envelope, with the redshifted velocity component appearing throughout most of the east side of the envelope. The redshifted velocity component (-4.0 km s^{-1}) begins to appear just before the PV cut crosses IRS1 (offsets from $-5''$ to $70''$), indicating that it could be related to the redshifted outflow from IRS1. However, the redshifted velocities continue as the cut follows the envelope southeast, well beyond the region of influence of the redshifted outflow from IRS1. The redshifted outflow of IRS2 is directed in this region and has substantial ^{12}CO and ^{13}CO emission that fans out toward the east side of the envelope. Thus, it is clear that the eastern side of the envelope has a second redshifted velocity component, but it is unclear if this is outflow-related or part of the cloud structure itself.

4.3. ALMA N_2D^+ Kinematics

With the ambiguity of the NH_3 kinematics near IRS1 and IRS2, higher resolution is imperative to distinguish the kinematic structure of gas surrounding the binary system.

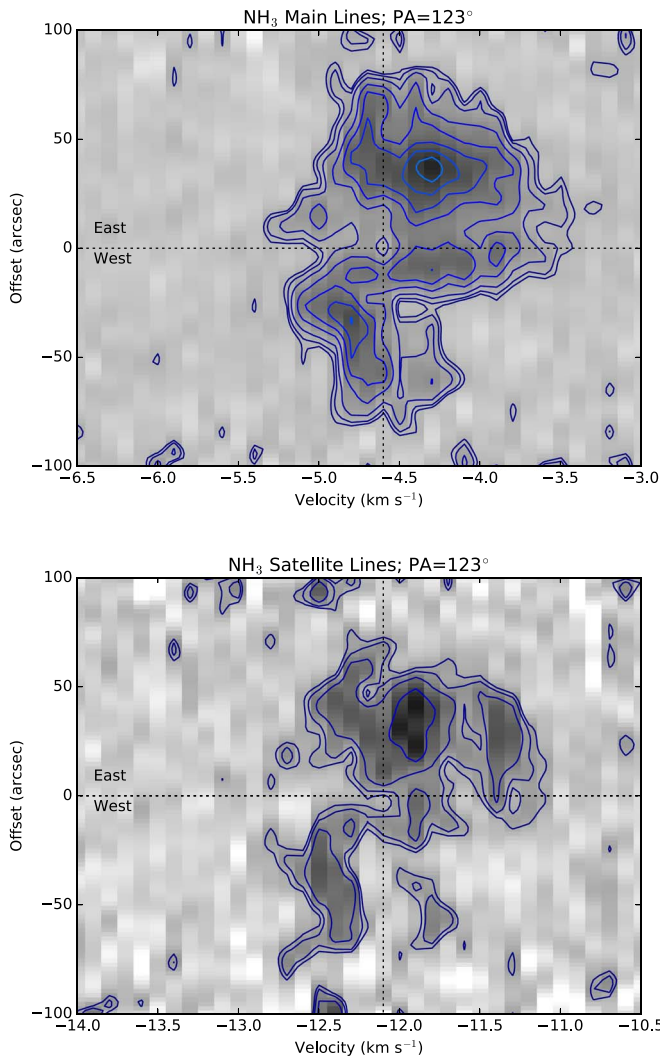


Figure 13. Position–velocity diagrams of NH_3 taken in a $10''$ wide strip along a position angle of 123° east of north, centered on IRS1. The extracted region is bounded by the dashed lines in the upper right panel of Figure 10. The top panel shows the PV diagram of the main NH_3 hyperfine lines, and the bottom panel shows a PV diagram of a set of NH_3 satellite hyperfine lines that are not as closely spaced as the main lines.

The ALMA observations include N_2D^+ ($J = 3 \rightarrow 2$); the deuterated form of N_2H^+ . N_2H^+ , N_2D^+ , and NH_3 have been shown in multiple studies to trace the same (or very similar) kinematic and physical structures in both starless and protostellar cores in single-dish and interferometric studies (Johnstone et al. 2010; Tobin et al. 2011). N_2D^+ has the caveat that it can be destroyed in the inner regions of the envelope where N_2H^+ and NH_3 can still exist (Tobin et al. 2013), but in the case of BHR71, the NH_3 and N_2D^+ peaks align closely with the N_2H^+ peaks found by Chen et al. (2008).

We show the N_2D^+ integrated intensity maps overlaid on the *Spitzer* $8\ \mu\text{m}$ image, the ATCA NH_3 , and the 1.3 mm continuum in Figures 15 and 16. The N_2D^+ map covers a smaller region than the ATCA NH_3 map; therefore N_2D^+ does not map to the $8\ \mu\text{m}$ absorption feature as well as NH_3 . However, there is good correspondence to the east of IRS1. N_2D^+ also tends to avoid the region of the outflow toward IRS1, but there is some emission north of IRS1 along the redshifted outflow. Toward IRS2, N_2D^+ does not clearly avoid the outflow, which might be due to the 3D configuration of the

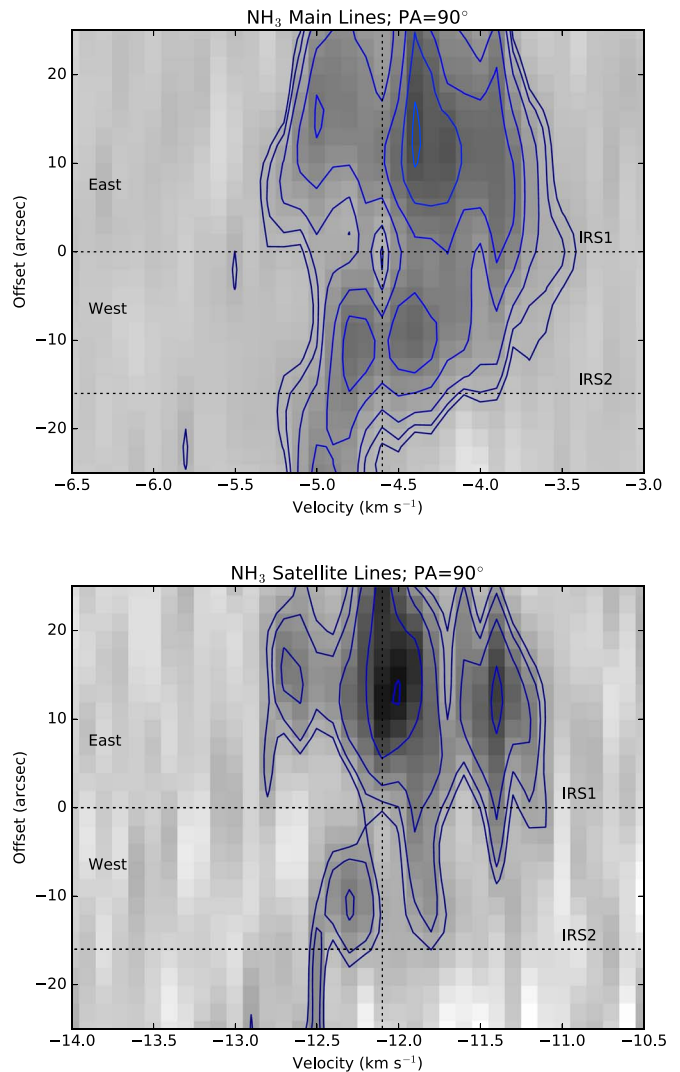


Figure 14. Position–velocity diagrams of NH_3 taken in a $10''$ wide strip in the east–west direction, centered on IRS1. The region extracted is bounded by the dashed lines in the upper right panel of Figure 11. The top panel shows the PV diagram of the main NH_3 hyperfine lines, and the bottom panel shows a PV diagram of a set of NH_3 satellite hyperfine lines that are not as closely spaced as the main lines.

envelope. Finally, the N_2D^+ east of IRS2 corresponds well to the NH_3 map, but east and south of IRS2, the NH_3 intensity drops, while N_2D^+ emission surrounds IRS2 on three sides. We also note in Figure 16 that the extended 1.3 mm continuum around IRS1 seems to avoid the brightest areas of N_2D^+ emission. Specifically, the extended emission west of IRS1 seems to run through the gap in N_2D^+ toward IRS2.

The kinematic structure is derived from the N_2D^+ data using the CLASS hyperfine fitting routines and the known hyperfine line positions and relative line ratios (Dore et al. 2004); also see Tobin et al. (2013); see the Appendix. The overall kinematic structure of N_2D^+ is quite similar to that of NH_3 in the overlapping regions, except that some of the velocity gradients are better resolved. There are also still indications of outflow-envelope interaction with redshifted line-center velocity south-east of IRS1 and increased line width in this region. In the N_2D^+ line-width map, the line width is remarkably low throughout the entire envelope. The map is slightly noisy because of the smaller beam and the lower signal-to-noise ratio

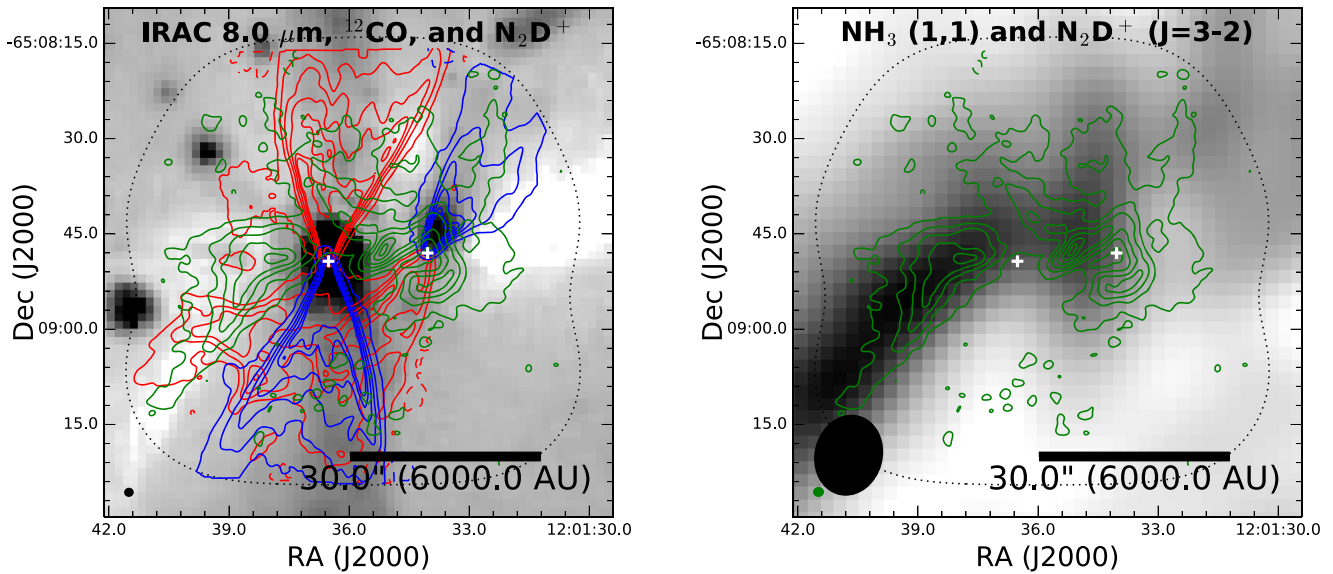


Figure 15. Integrated intensity contours from the ALMA N_2D^+ ($J = 3 \rightarrow 2$) observations overlaid (green) on the *Spitzer* $8.0 \mu\text{m}$ image (inverse grayscale) in the left panel and N_2D^+ is overlaid (green) on the ATCA NH_3 (1, 1) integrated intensity map (inverse grayscale) in the right panel. We also overlaid the ^{12}CO blue- and redshifted integrated intensity contours (with corresponding colors) from Figure 6. The extent of C^{18}O shown in Figure 6 is consistent with the size of the N_2D^+ deficit regions. There is some correspondence on the east side of the N_2D^+ and the $8 \mu\text{m}$ absorption of the envelope, but less than the ATCA NH_3 due to the smaller area mapped by ALMA. The ALMA N_2D^+ corresponds well with the NH_3 on the eastern side to the edge of the map, and the emission toward IRS1 is lower in both NH_3 and N_2D^+ . Near IRS2, the correspondence of N_2D^+ and NH_3 is not as close: the peak of NH_3 east of IRS2 corresponds with the N_2D^+ peak, but N_2D^+ east and south of IRS2 has lower NH_3 intensity. The N_2D^+ contours start at 5σ and increase in 10σ intervals, where $\sigma = 0.098 \text{ K km s}^{-1}$.

(S/N) in some regions. North of IRS1, there is still the large region of redshifted velocities that coincides with the likely area of influence from the outflow. Toward IRS2, the line-center velocity map is not highly structured, particularly away from the region of redshifted velocities that seems to be associated with IRS1. The velocity gradient around IRS2 appears to lie more along the outflow direction than orthogonal to it. Overall, the N_2D^+ line-center velocity near IRS2 is very close the line-center velocity to the east of IRS1. Thus, it is not clear that the kinematics strongly indicate rotation across the core on scales comparable to the protostar separation, or even around the protostars themselves. The area of large line width observed north of IRS2 in NH_3 with ATCA is not reflected in the N_2D^+ map, likely because this was due to a velocity gradient that is resolved in the ALMA map. Given that the velocities of the gas toward IRS2 and the gas east of IRS1 have comparable velocities, the kinematics surrounding IRS1 and IRS2 do not strongly indicate that they are forming out of kinematically distinct cores. The only firm conclusion that we can make is that the outflow from IRS1 appears to significantly affect the kinematic structure to the north.

The velocity profiles from the ALMA N_2D^+ velocity maps are also extracted along lines orthogonal to the outflow directions and shown in Figure 12. Compared to the ATCA NH_3 velocity profiles, the N_2D^+ profiles are significantly more structured, and the velocity away from the protostar position for IRS1 does not agree as closely with the Parkes velocities. This could result from chemical differences between N_2D^+ and NH_3 . Alternatively, the higher resolution of the N_2D^+ data could be resolving structure that is smoothed out in the lower resolution of the ATCA data.

In addition to the line-center velocity maps and profiles, we also extracted a PV diagram from the N_2D^+ emission toward BHR71. This PV diagram is shown in Figure 17 and is taken in an east–west cut $10''$ in width, centered on IRS1. The angular resolution of the N_2D^+ maps is about five times finer than the

NH_3 map, so some features appear different, but the major features are similar. The PV cut of N_2D^+ shows very little evidence for a systematic velocity gradient across the position of IRS1. A second velocity component is also still evident (-4.0 km s^{-1}), but this redshifted component is most evident near the protostar position at an offset position of $\pm 5''$. The redshifted velocity component is made less obvious because the brightest hyperfine lines are spread over $\sim 0.5 \text{ km s}^{-1}$ (Dore et al. 2004), in contrast to the pairs of ammonia lines that are less strongly blended. The lines also appear slightly more redshifted than NH_3 because we assigned the rest frequency to match the brightest N_2D^+ hyperfine line, which is at a higher frequency than the other hyperfine lines of comparable relative intensity.

4.4. ALMA C^{18}O Kinematics

Inside the N_2D^+ and NH_3 emitting regions, we find that C^{18}O emission peaks directly on the continuum sources, as shown in Figure 6. There is also extended emission around IRS1 and IRS2, but with most emission concentrated at the location of the continuum sources. Moreover, toward IRS1, the C^{18}O appears extended along the walls of the outflow cavities. A thin ridge of increased C^{18}O brightness also extends between IRS1 and IRS2.

We examined the C^{18}O line kinematics for signs of rotation, infall, and/or outflow entrainment by first examining the integrated intensity, line-center velocity, and line-width maps shown in Figure 18. These are similar to the maps constructed for the NH_3 and N_2D^+ data, but instead of fitting the hyperfine lines, we calculated the standard first- (centroid velocity) and second- (line width) moment maps because C^{18}O is a single-emission line. The centroid velocity map shows the signature of the outflow from IRS1, but there is a very slight “twist” in the velocity map across the source, indicating that there is more going on than just the outflow. The line-width map also shows a

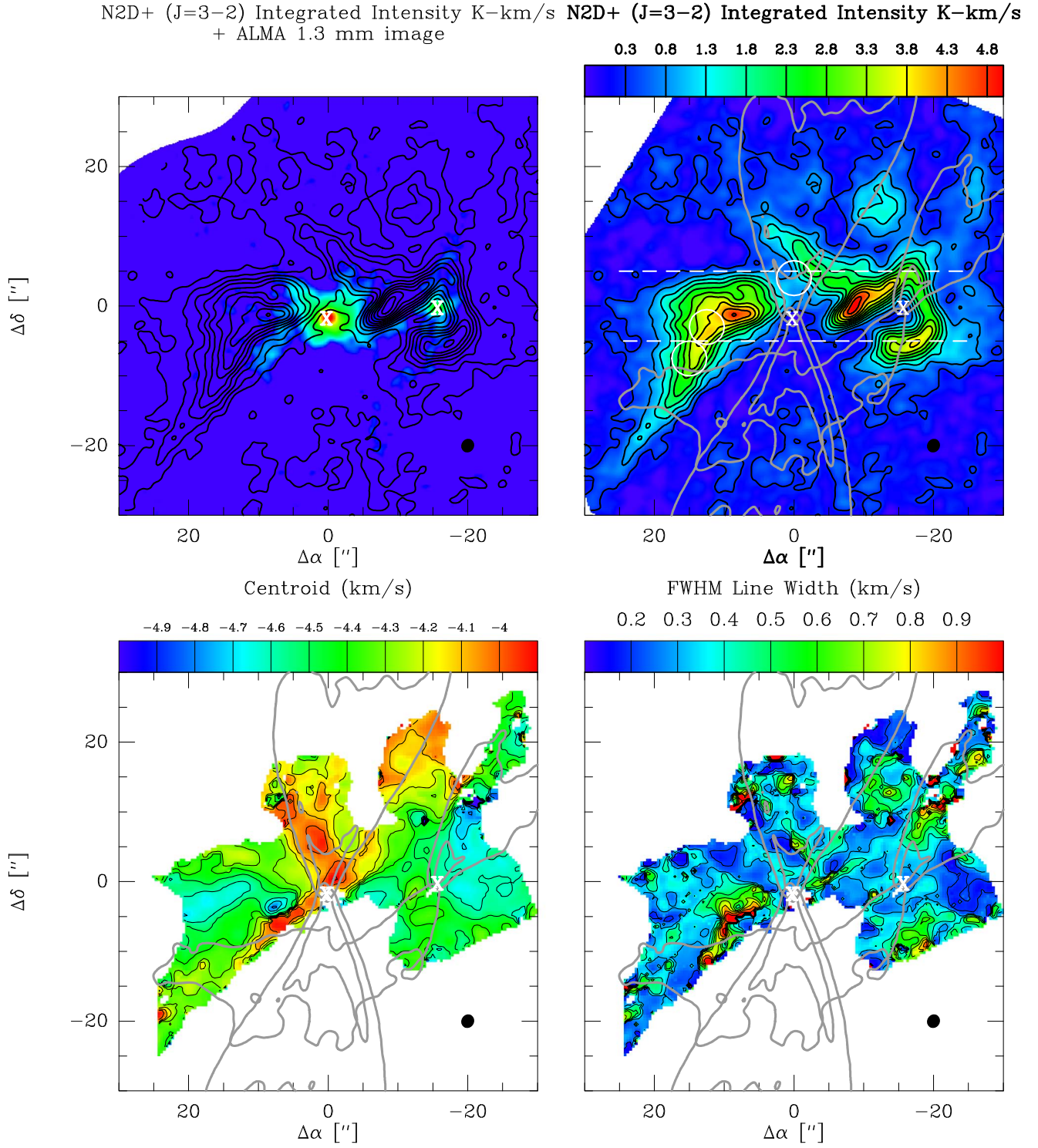


Figure 16. Same as for Figure 10, but for the ALMA N₂D⁺ ($J = 3 \rightarrow 2$) transition, and the data are overlaid on the ALMA 1.3 mm image instead of on the *Spitzer* 8 μ m image. The spatial extents of the outflows probed by ALMA in ¹²CO are marked with the gray contours in all panels except for the top left panel. The integrated intensity maps show clear deficits of N₂D⁺ toward the protostar locations, as expected from protostellar heating. However, toward IRS2, N₂D⁺ is found in a horseshoe-shaped feature. The velocity structure is markedly different, it reaches lower velocities on the eastern side of the envelope in N₂D⁺ vs. NH₃. Some of this is likely due to the higher resolution of the ALMA data, and there is not as much blending of line components. Here the more redshifted features to the north appear to occupy a greater area than the outflow region of influence delineated by the ¹²CO contours. Ignoring the features on the north side of the envelope, the east and west side of the envelope are at practically the same velocity. The line-width map is very noisy due to the low S/N in some parts of the data, but the line widths are all quite narrow, much more narrow than NH₃ in most places. The intensity levels in the top panels are from the integrated intensity map of the main hyperfine lines between -5.5 to -3.7 km s⁻¹; the intensity levels start at 3σ and increase in 5σ intervals, where $\sigma = 0.1$ K km s⁻¹. The dashed lines in the upper right panel denote the region of PV extraction, and the dashed circles in the upper right panel correspond to regions of spectral extraction to examine the quality of hyperfine fitting, see the [Appendix](#).

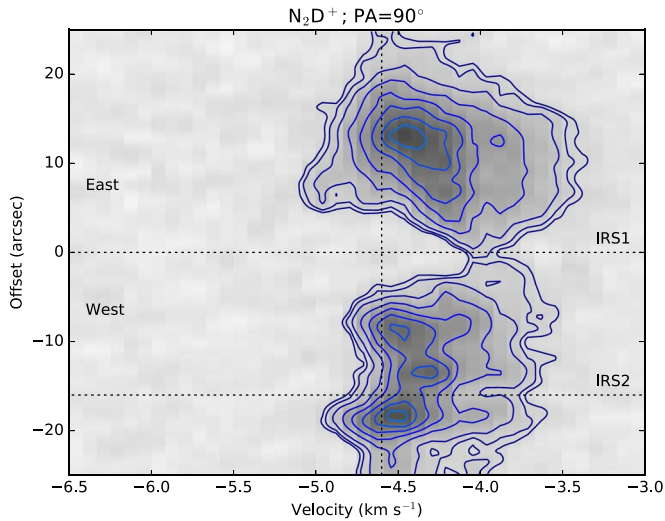


Figure 17. Position–velocity diagram of N_2D^+ emission toward IRS1 and IRS2 taken in a $10''$ cut across the equatorial plane of the envelope ($\text{PA} = 90^\circ$), centered on IRS1. The region extracted is bounded by the dashed lines in the upper right panel of Figure 16. The second velocity component shown in Figure 14 is difficult to discern because the hyperfine structure of N_2D^+ ($J = 3 \rightarrow 2$) is comprised of closely spaced lines with comparable relative intensities. The overall emission is more broad on the east side of the envelope than on the west due to the additional velocity component, however. The redshifted velocities related to the outflow are clear at the position of IRS1, where the only detectable emission is redshifted. The overall line profiles are more strongly shifted toward the red because the rest frequency of our observation was centered on the brightest hyperfine line of N_2D^+ ($J = 3 \rightarrow 2$), which is located at a slightly higher frequency than most of the other lines with a comparable relative intensity.

broadener line width near the position of IRS1, which is indicative of more rapid motion along the line of sight. There is no evidence of an enhanced line width toward IRS2, but moment maps are most often dominated by the low-velocity emission that is strongest, especially in the case of a map that includes total power emission (Figure 7).

In order to better examine the motions of the gas near the protostar positions, we examine integrated intensity maps constructed using only the higher velocity blue- and redshifted emission independently. Toward IRS1, integrated intensity maps are shown in Figure 19 for the red- and blueshifted C^{18}O in velocity ranges from low (-5.8 to -4.4 km s^{-1} and -4.4 to -3.2 km s^{-1}), medium (-6.2 to -5.6 km s^{-1} and -3.6 to -2.8 km s^{-1}), and high (-6.3 to -5.8 km s^{-1} and -3.0 to -2.5 km s^{-1}) velocity. At lower velocities, the red- and blueshifted emission are clearly offset along the outflow direction. At medium velocities, the emission becomes more compact and the red- and blueshifted emission is oriented diagonally across the continuum source, possibly tracing both outflow and motion in the equatorial plane. We also note that velocity gradients in the direction of the outflow may result from infall motion (Yen et al. 2013), but may also be related to outflow-envelope interaction (Arce & Sargent 2006).

C^{18}O at the highest velocities has blue- and redshifted emission peaks that are oriented in the east–west direction (blue to the east, and red to the west), with some low-level emission along the outflow direction. Thus, this velocity gradient is oriented perpendicular to the outflow, as expected for rotational motion on <1000 au scales in the inner envelope. Note that the direction of this velocity gradient is opposite of what is observed on large scales with Parkes and ATCA.

The C^{18}O emission toward IRS2, on the other hand, is found to have the redshifted peak to the east and the blueshifted peak is to the west (Figure 20). The position angle is not exactly orthogonal to the outflow, but it is not along the outflow either. Thus, the small-scale velocity gradients in C^{18}O appear to be in the opposite directions for IRS1 and IRS2.

To examine the kinematics in more detail, we show PV diagrams of the C^{18}O emission toward IRS1 and IRS2 in Figure 21. These PV cuts are taken orthogonal to the outflow directions of each source, centered on the continuum source. For both sources, positive offsets are to the east and negative offsets are to the west. The PV diagrams in Figure 21 are generated using only the data from the ALMA 12 m array to reduce confusion with the extended emission picked up by the ACA and total power observations.

The PV diagram for IRS1 shows that at high velocities near the continuum position, the blueshifted side is located to the east and the redshifted side is located to the west. Toward lower velocities, the C^{18}O emission is more symmetrically distributed in both position and velocity. IRS2 shows a considerably different appearance. First, the C^{18}O is not as spatially extended, likely because IRS2 is ten times less luminous than IRS1, and the emitting region is expected to be smaller. Second, the region with the brightest blueshifted C^{18}O is still on the west side of the envelope, while the brightest redshifted C^{18}O is on the east side of the envelope. Thus, both in the integrated intensity maps and the PV diagrams, the velocity gradients of IRS1 and IRS2 are in the opposite direction.

The PV diagrams also show that the C^{18}O emission of the protostars is slightly different from the velocity of the core. The C^{18}O emission is best described with a central velocity of -4.6 km s^{-1} , in contrast to the average core velocity of -4.45 km s^{-1} from Parkes NH_3 emission. Parts of the core also show velocities that are even more different: Figure 16 shows that the core near IRS2 and east of IRS1 has velocities up to -4.9 km s^{-1} , and near IRS1 the velocity can be -4.2 km s^{-1} .

To compare the PV diagram of the C^{18}O emission to that of the NH_3 and N_2D^+ , we used the 12m+ACA+TP data to show the PV diagram on comparable spatial scales across both sources and show this larger-scale C^{18}O PV diagram in Figure 22. The PV diagram shows that there is extended structure from the surrounding core toward both IRS1 and IRS2. Similar to NH_3 and N_2D^+ , the C^{18}O shows an apparent second velocity component around -4.0 km s^{-1} that is present from $-25''$ to beyond $30''$. However, the protostars themselves seem to be more closely associated with the blueshifted velocity component. The blueshifted component is at about -4.9 km s^{-1} and the protostars are between -4.7 and -4.6 km s^{-1} . We note, however, that the large-scale C^{18}O emission likely reflects the velocity of the gas in the exterior regions of the cloud because C^{18}O is likely frozen out onto dust grains in the higher-density interior of the core/envelope where N_2D^+ and NH_3 are present (Frerking et al. 1982; Benson & Myers 1989).

5. Discussion

As an isolated core harboring a wide binary system, BHR71 should lend itself to being an ideal testing ground for wide binary formation. The formation of such systems has long been thought to be related to the rotation of the core (e.g., Larson 1972; Boss & Bodenheimer 1979; Burkert &

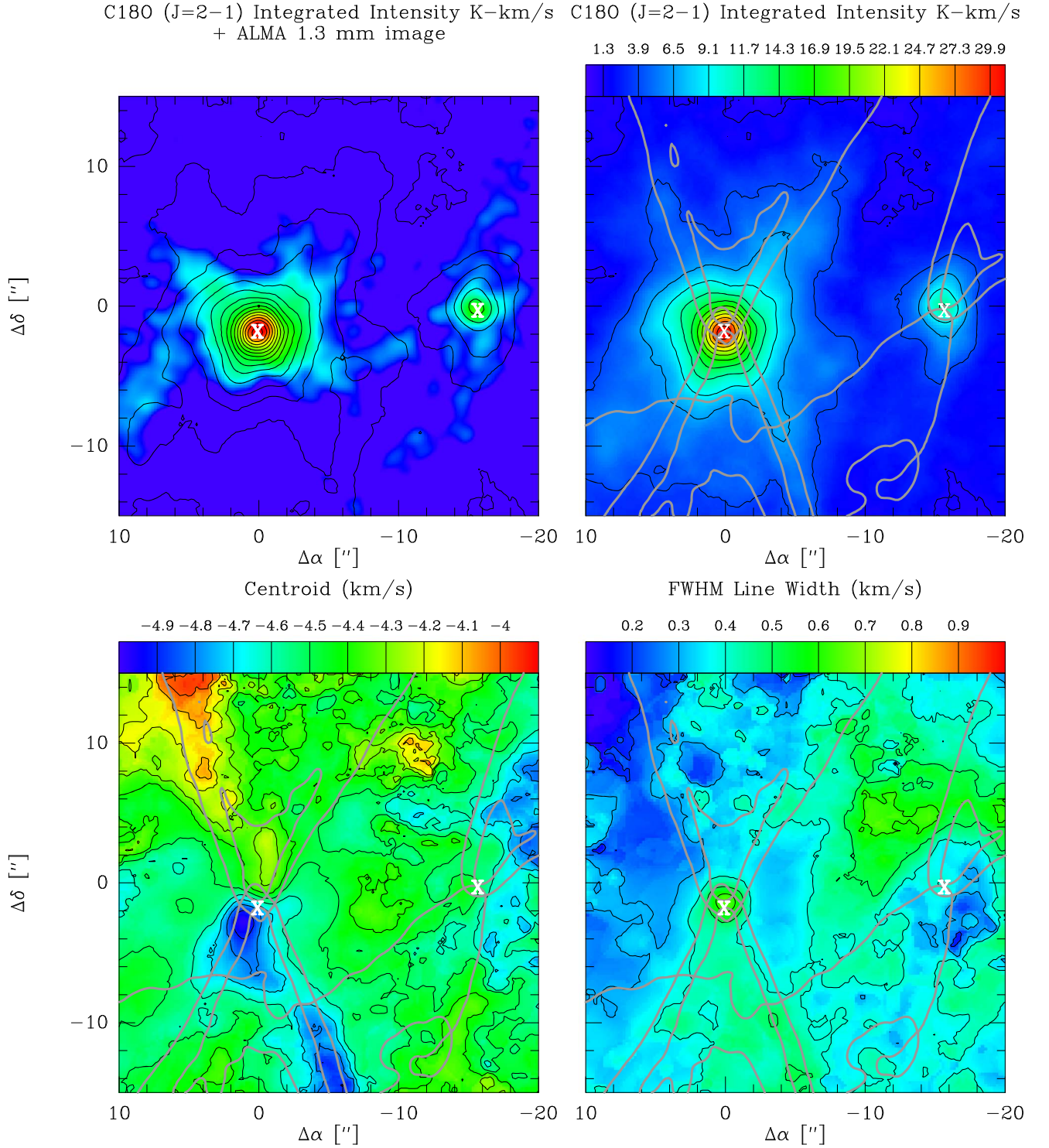


Figure 18. Same as for Figure 16, but for the ALMA C¹⁸O ($J = 2 \rightarrow 1$) and zoomed-in on a smaller area centered on the two protostars. The line-center velocity map in the lower left panel shows the clear influence of the outflow on the C¹⁸O kinematics, but there is a twist near the location of the protostar that is inconsistent with the outflow. The line-width map for C¹⁸O shows an enhanced line width toward IRS1, which is indicative of more rapid motion along the line of sight; IRS2 does not show an increased line width. The intensity levels shown are the same as in Figure 6, using the 12m+ACA+TP data.

Bodenheimer 1993; Tohline 2002). Thus, our initial expectation was to find a classic scenario of clear core rotation, with conserved angular momentum leading to increased rotation velocity at progressively smaller radii. We also expected that a difference in radial velocity of IRS2 relative to IRS1 due to orbital motion could be measured because of its separation, lower overall luminosity, and estimated dust+gas mass.

5.1. Kinematic Analysis

The kinematic structure observed in NH₃ from Parkes and ATCA alone appeared remarkably consistent with rotation-induced fragmentation. The Parkes data showed a modest velocity gradient on arcminute scales, and the ATCA data showed evidence of a larger velocity gradient across the two

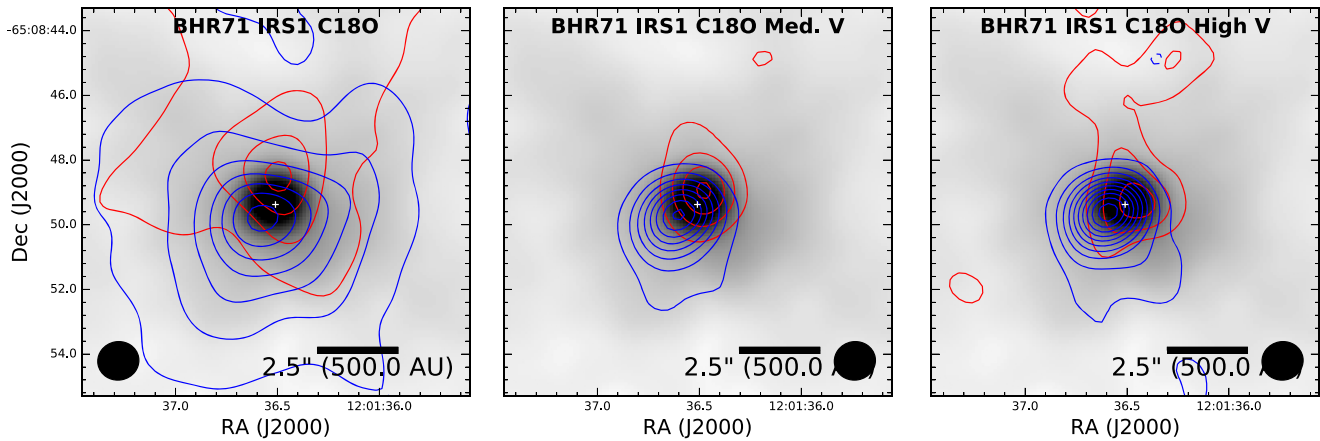


Figure 19. C^{18}O red- and blueshifted integrated intensity maps toward IRS1 (using 12m+ACA+TP data) shown in different velocity ranges and overlaid on the 1.3 mm continuum image. The low-velocity C^{18}O clearly is influenced by the outflow, but at moderate and higher velocities, the C^{18}O begins to trace a velocity gradient orthogonal to the outflow, the expected velocity gradient direction for rotation. The low-velocity emission is integrated between -5.8 to -4.4 km s^{-1} and -4.4 to -3.2 km s^{-1} , and $\sigma_{\text{red,blue}} = 0.09, 0.1$ K km s^{-1} , and the contours are drawn starting at 30σ and increase in intervals of 30σ . The moderate-velocity emission is integrated between -6.2 to -5.6 km s^{-1} and -3.6 to -2.8 km s^{-1} , and $\sigma_{\text{red,blue}} = 0.08, 0.07$ K km s^{-1} , and the contours are drawn starting at 10σ and increase in intervals of 10σ . The high-velocity emission is integrated between -6.3 to -5.8 km s^{-1} and -3.0 to -2.5 km s^{-1} , and $\sigma_{\text{red,blue}} = 0.06, 0.06$ K km s^{-1} , and the contours are drawn starting at 3σ (5σ) and increase in intervals of 3σ (5σ); the values in parentheses correspond to the blue contours. The 12m+ACA+TP data were used to generate this figure.

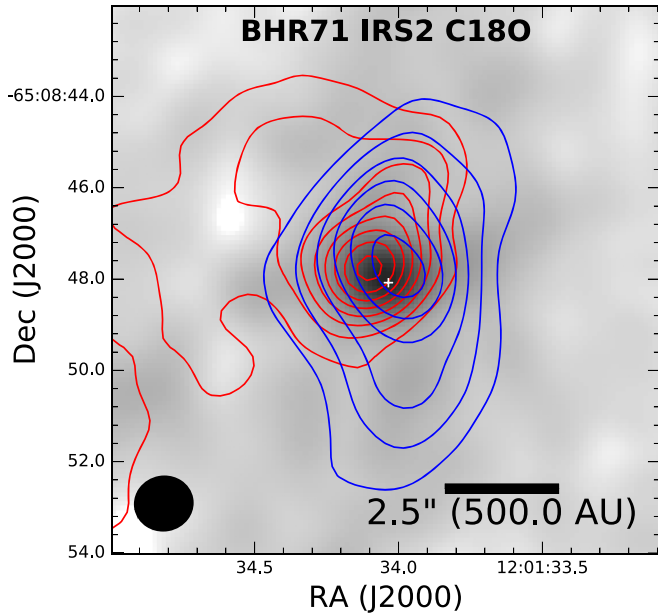


Figure 20. C^{18}O red- and blueshifted integrated intensity maps toward IRS2 (using 12m+ACA+TP data). A velocity gradient is evident, in a direction that is nearly orthogonal to the outflow. However, the velocity gradient direction is in the *opposite* sense with respect to the gradient direction in IRS1. The C^{18}O emission is integrated between -5.1 to -4.4 km s^{-1} and -4.4 to -3.5 km s^{-1} , and $\sigma_{\text{red,blue}} = 0.08, 0.074$ K km s^{-1} . The red and (blue) contours are drawn starting at 15σ (35.0σ) and increase in intervals of 5σ (10σ).

protostars. Furthermore, previous ATCA N_2H^+ observations toward IRS1 detected a velocity gradient across the main protostar, but did not detect emission around IRS2 due to the smaller primary beam at 3 mm (Chen et al. 2008). The velocity gradient observed by Parkes along the major axis of the core as viewed in NH_3 is 1.2 $\text{km s}^{-1} \text{ pc}^{-1}$, measured across a diameter of $150''$ ($30,000$ au). The low resolution of the single-dish observations smooths out any velocity structure at small scales and provides a measure of the velocity gradient on the largest scale, which for the sake of this discussion, we interpret as solid-body rotation. When material is in free fall, however,

rotation no longer is solid-body rotation and conserves angular momentum (in the absence of magnetic fields). This gradient would correspond to a rotation velocity of 0.087 km s^{-1} at the core radius of $15,000$ au and an angular velocity (Ω) of 3.9×10^{-14} s^{-1} . If we assume that the entire core at radii smaller than $15,000$ au is in free fall, the infalling gas should conserve angular momentum. Then, the rotation velocity should be ~ 0.33 km s^{-1} at a radius of 4000 au. At the separation of IRS2, $16''$ (3200 au), the rotation rate would be even higher, 0.4 km s^{-1} . The ALMA N_2D^+ map shows very little evidence of a velocity gradient of this magnitude from the area directly east of IRS1 to the area surrounding IRS2. Furthermore, the C^{18}O velocities of IRS1 and IRS2 are consistent with being at the same velocity. The lack of observed rotation velocity on 3200 au scales, however, could be due to the apparent influence of the outflow on the ambient envelope material, masking hints of rotational velocity increases toward the envelope center. The largest scales examined by the ALMA N_2D^+ do not show ordered rotation surrounding either IRS1 or IRS2, however.

In the preceding paragraph, we assumed that the entire core was falling in and that only the velocity gradient on the largest scales reflected solid-body rotation. If we instead assume that the entire core is not yet collapsing and the 1.2 $\text{km s}^{-1} \text{ pc}^{-1}$ velocity gradient reflects solid-body rotation out to a certain radius, then we can calculate different rotation velocities. Assuming inside-out collapse (Shu 1977; Terebey et al. 1984), the infall radius must be larger than the companion separation. If we assume an infall radius of 6400 au, twice the companion separation, the solid-body rotation velocity at this radius would be 0.037 km s^{-1} with 1.2 $\text{km s}^{-1} \text{ pc}^{-1}$ gradient ($\Omega = 3.9 \times 10^{-14}$ s^{-1}), which is below our ability to detect. Furthermore, if angular momentum was conserved from a hypothetical infall radius of 6400 au, then the rotation velocity at a radius of 3200 au would only be 0.074 km s^{-1} . Both the solid-body rotation rate at 6400 au and the estimated rotation velocity from conserved angular momentum at 3200 au would be below our ability to detect. Nevertheless, the core is observed to have a velocity structure with significantly larger

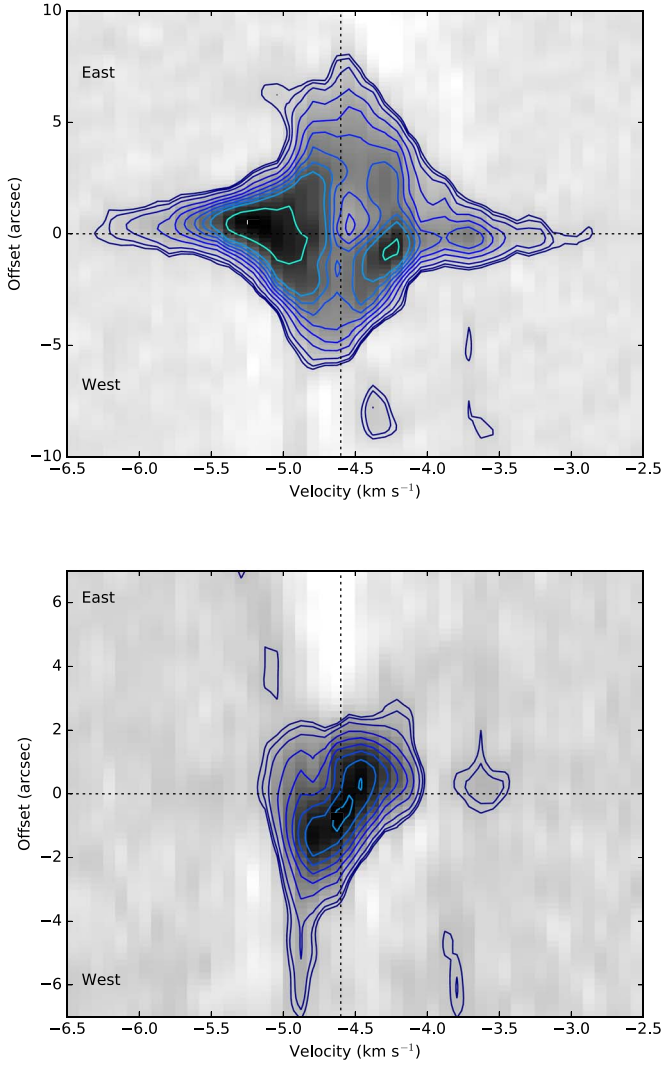


Figure 21. Position–velocity diagrams of C^{18}O emission toward IRS1 (top) and IRS2 (bottom) taken in cuts orthogonal to the outflow directions, $6''.2$ in width. The velocity gradient in IRS1 appears to extend from the upper left quadrant to the lower right quadrant at the highest velocities, and the velocity gradient in IRS2 appears to extend from the lower left quadrant to the upper right quadrant. The two PV diagrams are generated using only the data from the ALMA 12 m array, excluding the ACA and total power. This limits confusion from the inclusion of the extended C^{18}O emission.

amplitudes than these extrapolations from the large-scale core rotation. These inconsistencies can be taken as evidence against an ordered collapse of the system with rotationally induced fragmentation.

Using these observationally measured quantities of the core velocity structure, we can calculate the estimated stability of the core from the ratio of rotational energy to gravitational potential energy (β_{rot}) on the scale of 3200 au. While this diagnostic assumes solid-body rotation and we use a rotation velocity inferred from the assumption of constant angular momentum, this analysis enables comparisons to other studies that determine β_{rot} as their key diagnostic derived from the observations. We follow the method outlined by Chen et al. (2007), who calculated the rotational energy as

$$E_{\text{rot}} = \frac{1}{2} I \Omega^2 = \frac{1}{2} \alpha_{\text{rot}} M R^2 \Omega^2 \quad (2)$$

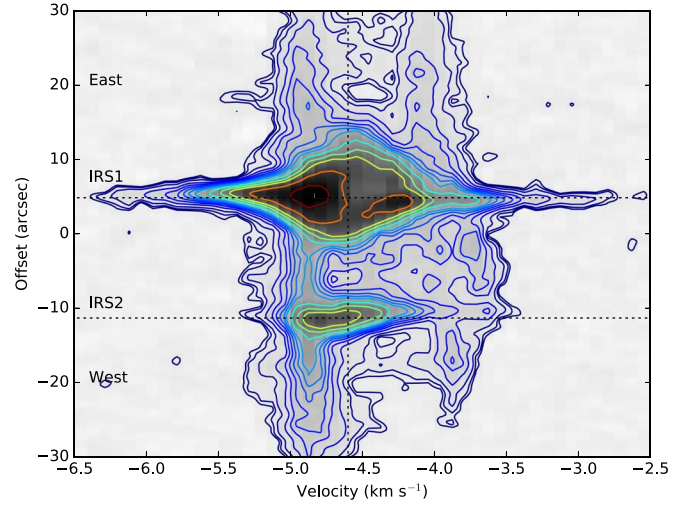


Figure 22. Position–velocity diagrams of C^{18}O emission encompassing both IRS1 and IRS2 taken in the same cut as the NH_3 and N_2D^+ PV diagrams shown in Figures 12 and 17. This PV diagram includes the 12 m, ACA, and total power data to recover the extended structure from the core. Similar to NH_3 and N_2D^+ , C^{18}O also shows two velocity components, one at about -4.9 km s^{-1} and the other at about -4.0 km s^{-1} . The C^{18}O emission concentrated around the protostars themselves is somewhat between the two velocity components, but more closely associated with the blueshifted velocity component, having their velocity centers at about -4.6 km s^{-1} .

and $\alpha_{\text{rot}} = \frac{2}{3}(3 - p)/(5 - p)$, Ω is the angular velocity derived from the observed velocity gradient, R is the radius of the envelope, and M is the mass of the envelope. We adopt $p = 1.5$ for a spherical envelope in free fall. Note that this is not exact because the envelope around BHR71 IRS1 and IRS2 is non-spherical. Then the gravitational binding energy is defined from the virial theorem to be

$$E_{\text{grav}} = \frac{3GM^2}{5R}, \quad (3)$$

where G is the gravitation constant; M and R are the same as defined for the previous equation. Knowing these two equations, β_{rot} can be calculated

$$\beta_{\text{rot}} = \frac{E_{\text{rot}}}{E_{\text{grav}}} = \frac{5R^3 \Omega^2 \alpha_{\text{rot}}}{6GM}. \quad (4)$$

We can simplify this relationship by multiplying constants through and converting the more natural observed units such as solar masses, parsecs, and $\text{km s}^{-1} \text{ pc}^{-1}$, yielding

$$\beta_{\text{rot}} = 55.2 \left(\frac{R}{\text{pc}} \right)^3 \left(\frac{M_{\text{env}}}{1.0 M_{\odot}} \right)^{-1} \left(\frac{v_{\text{grad}}}{\text{km s}^{-1} \text{ pc}^{-1}} \right)^2. \quad (5)$$

The terms of the equation are now defined as R being the core radius in pc, v_{grad} is the velocity gradient in terms of $\text{km s}^{-1} \text{ pc}^{-1}$ across this scale, and M_{env} is the core/envelope mass in solar masses. We are interested in determining the level of rotational support both at a radius of 0.05 pc (10,000 au) to assess the level of rotational support in the envelope as a whole and at a radius of 3200 au (0.016 pc), the separation of IRS1 from IRS2. We first calculate β_{rot} for the larger scale using the velocity gradient measured across the BHR71 core of $\sim 1.2 \text{ km s}^{-1} \text{ pc}^{-1}$ and an envelope mass of $\sim 4.6 M_{\odot}$ determined for the radius of 0.05 pc

from 8 μm extinction from Tobin et al. (2010b). With these values, we find $\beta_{\text{rot}} = 0.002$ at a radius of 0.05 pc.

To calculate an upper limit of rotational support on the scale of the companion separation (3200 au; 0.016 pc), we assume that angular momentum is conserved and that the velocity gradient is more rapid at a radius 0.016 pc. Scaling the velocity gradient from the ratio of core to separation/inner envelope radius, the velocity gradient at a radius of 0.016 pc (3200 au) is $4.83 \text{ km s}^{-1} \text{ pc}^{-1}$. We then use the mass measured from the ALMA continuum data for both IRS1 and IRS2, which totals $0.7 M_{\odot}$, factoring in the likely higher dust temperature toward IRS1. With these numbers, we calculate an upper limit to $\beta_{\text{rot}} = 0.006$. Note that we call this an upper limit because we assumed that angular momentum was conserved from larger scales, but the velocity gradient across the envelope from ALMA N_2D^+ is consistent with zero. Furthermore, Tobin et al. (2011, 2012b) argued that for elongated envelopes such as BHR71, projected infall motions can contribute to the observed velocity gradients. Last, if the motions do correspond to rotation, inclination is not taken into account, therefore rotation could be higher if that is the origin of the velocity gradient. However, as outlined in Section 3.3, the inclination of the outflows is very likely greater than 35° , therefore the correction to the rotation velocity is likely less than a factor of 2. The $\beta_{\text{rot}} = 0.006$ measurement for BHR71 places this system toward the top end of the distribution of single systems shown in Chen et al. (2012). However, this might not be an entirely fair comparison because these β_{rot} values are calculated at a variety of core radii, some single dish and some interferometric. We further emphasize that if we evaluate the velocity gradient from the ALMA N_2D^+ , excluding the regions that are likely outflow influenced, β_{rot} could be much lower. Our calculated value for β_{rot} is lower than the one determined by Chen et al. (2008), but these authors probed a different scale focused on IRS1 using N_2H^+ .

In addition to the apparent velocity gradients, the observations also revealed the presence of two velocity components of the dense gas to the east of IRS1. The NH_3 and N_2D^+ line-center velocities are distinctly redshifted in the regions that overlap with the redshifted outflow lobe of IRS1. Furthermore, the PV diagrams shown in Figures 12, 17, and 22 show that this redshifted component is also present in the equatorial plane of the envelope. Its presence in the equatorial plane is diminished in the velocity maps that are derived from hyperfine fitting of the NH_3 and N_2D^+ in Figures 10, 11, and 16 because the blueshifted component has a greater line strength.

This additional line component must not be very broad since it can be observed as a distinct component in the PV diagrams in Figures 12, 17, and 22. The outflow from IRS1 could be inducing bulk motion in the surrounding molecular gas, similar to the simulations of Offner & Arce (2014). Furthermore, the redshifted lobe of the outflow from IRS2 could also be contributing to the redshifted velocities in NH_3 and N_2D^+ on the southeast side of the envelope. The overlap of IRS2 outflow contours in Figures 10, 11, and 16 highlights this possibility, although the region is also coincident with the edge of the blueshifted outflow cavity from IRS1. Alternatively, the two velocity components could also result from velocity shear that might have been present during the formation of a core. However, the ambiguity of the formation conditions of the BHR71 core and its structure along the line of sight makes the origin of the second velocity component and the interaction

of the outflows and dense molecular gas difficult to confidently ascertain.

5.2. Formation of the Binary System

Models that consider the formation of multiple star systems from rotating collapsing envelopes have difficulty fragmenting for parameters similar to the observed quantities of β_{rot} and Ω for BHR71. One of the classic studies of Burkert & Bodenheimer (1993) used a rotating collapsing envelope with an $m = 2$ perturbation to break the symmetry. However, they still needed a fairly rapid rotation rate for fragmentation on >1000 au scales, using $\Omega = 7.2 \times 10^{-13} \text{ s}^{-1}$, resulting in $\beta_{\text{rot}} = 0.16$. Thus, these models had over an order of magnitude more rotation in order to produce fragmentation on the desired scale.

Recent work by Boss & Keiser (2014) explored fragmentation with rotating cloud cores including magnetic fields. This work did not find fragmentation on scales >1000 au for systems with rotation rates $<10^{-13} \text{ s}^{-1}$ nor $\beta_{\text{rot}} < 0.01$. The systems that most frequently produced fragments on scales >1000 au in these simulations had the highest rotation rates ($\Omega = 3 \times 10^{-13} \text{ s}^{-1}$). Systems still fragmented in the presence of magnetic fields, but the models with the strongest magnetic fields did inhibit fragmentation. Many other models considering core rotation also had difficulty in forming multiple systems with >1000 au for rotation rates comparable to or exceeding those found in our observations (e.g., Price & Bate 2007; Machida et al. 2008).

Adding all this information on the kinematics of BHR71 together and combining it with recent numerical studies of multiple star formation with rotation, we find it unlikely that core rotation could have resulted in the formation of the binary system. This is based on the reasonable upper limit to the value of $\beta_{\text{rot}} = 0.006$, but in reality, the core rotation is nearly zero across the inner envelope, as probed by N_2D^+ and toward the protostars as measured with C^{18}O . More to the point, the overall inner envelope kinematics are not consistent with ordered rotation when viewed with NH_3 and N_2D^+ at high enough resolution to both resolve the companion and recover the extended emission of the envelope. However, regardless of the level of true rotation in BHR71, the evidence for rotation in the opposite direction on scales <1000 au cannot be easily reconciled. On the scales of disks, the Hall effect could theoretically reverse the direction of rotation in the disk (Krasnopolsky et al. 2010; Tsukamoto et al. 2015), but the motions we observe are on >100 s of au scales where the densities should not be high enough for non-ideal magnetohydrodynamics (MHD) effects to operate efficiently (Krasnopolsky et al. 2010).

Because of the observational inconsistencies with angular momentum conservation and the difficulty of simulations with similar initial conditions to result in wide companion formation, we must consider alternative scenarios for the formation of this binary system. One of the leading alternatives is turbulent fragmentation of the core (Padoan & Nordlund 2002; Goodwin et al. 2004; Offner et al. 2010). The turbulent velocity structure of the simulated molecular clouds will create density perturbations throughout the cloud. This creation of overdensities can be efficient enough such that these regions of locally enhanced density exceed the Jeans mass and collapse to become a protostar. Thus, a protostellar core or two adjacent cores formed in the presence of turbulence could lack an

ordered rotation pattern and still form a binary system. Simulations find that the initial separations of these cores are typically >500 au to 1000s of au (Offner et al. 2010; Bate 2012).

The apparent rotation in opposite directions on small scales for IRS1 and IRS2 can also result from turbulent fragmentation. Fragmentation can occur in a turbulent cloud without rotation of the envelope/core, and the angular momenta of the collapsing regions will be derived from the net angular momenta in the turbulent velocities (Offner et al. 2010, 2016; Walch et al. 2010). The net angular momenta of the density enhancements that formed IRS1 and IRS2 could have been anti-aligned, leading to the opposite rotation directions observed on <1000 au scales toward IRS1 and IRS2. Turbulent fragmentation is found to be quite likely for other widely separated protostellar multiple systems as well (Pineda et al. 2015; Lee et al. 2017).

The disordered velocity structure of the envelope as viewed in N_2D^+ and NH_3 could also be the result of turbulence in the core, where the bulk motion of turbulent gas could manifest itself as a disordered velocity structure. We suggest this because the outflow is unlikely to produce all the disordered velocity structure that is observed in the core. Specifically, we refer to the area east of IRS1 as shown in Figure 16, where the velocity along the north–south direction changes from redshifted to blueshifted and back to redshifted.

The misaligned angular momentum vectors are not unique to the BHR71 system. The Class 0 proto-multiple system IRAS 16293-2422 may have misaligned kinematics in its binary system separated by only ~ 600 au (e.g., Zapata et al. 2013), the IRAS 04191+1523 system with a separation of ~ 860 au has projected angular momentum vectors that differ by $\sim 90^\circ$ (Lee et al. 2017), and there are more evolved protoplanetary disk systems that also show similar misalignment (Stapelfeldt et al. 2003; Jensen & Akeson 2014; Williams et al. 2014; Brinch et al. 2016). Thus, the formation of multiple systems with misaligned or even anti-aligned angular momentum vectors may be common (Lee et al. 2016).

Despite the apparent consistency with turbulent fragmentation, many of the simulations are focused on fragmentation within a parsec-scale molecular cloud. However, BHR71 is an isolated core and is not located within a larger cloud (Bourke et al. 1995b). It is therefore unclear if the results from turbulent fragmentation are directly applicable. However, Walch et al. (2010) examined the effects of turbulence within isolated cores that are similar in size and mass to BHR71. They found that the turbulence within the core could lead to non-axisymmetric structure and misaligned net angular momenta. These particular simulations used very high levels of initial turbulence, however: the ratio of turbulent to gravitational binding energy in the simulated cores was between ~ 0.3 to ~ 0.6 . Following Walch et al. (2012), BHR71 has a ratio of turbulent to gravitational energy of ~ 0.04 , consistent with other star-forming cores. Therefore, the levels of internal turbulence do not appear sufficient to fragment the core in the way that it occurs in the study of Walch et al. (2010). Offner & Arce (2014) also examined isolated turbulent cores in their outflow study; however, fragmentation in those simulations was not witnessed on scales comparable to BHR71 IRS1 and IRS2, but that was also not the focus of their study.

A variation on the theme of turbulent fragmentation is that the shape of the core itself could cause multiple protostars to

form. Bonnell & Bastien (1993) considered the collapse of cylindrical cloud cores, and due to the shape, the ends of the cylinder collapsed first and formed two protostars. These protostars later moved closer together under their mutual gravitational attraction and formed a bound system. The fact that the BHR71 core appears elongated and asymmetric is similar to such a scenario. Moreover, molecular clouds themselves and even individual protostellar envelopes are often filamentary (e.g., Looney et al. 2007; André et al. 2010; Tobin et al. 2010a). It is therefore possible that the cloud shape played a role in the formation of BHR71 IRS1 and IRS2, but an asymmetric cloud (or portions of it) can only collapse if they are Jeans unstable.

While turbulent fragmentation can explain many of the features we observe in the velocity field, thermal Jeans fragmentation is another possible route for the formation of the binary system. If the gas is cold and dense, it can collapse without rotation or turbulent motions. Such a scenario is consistent with the lack of radial velocity shift between the sources. However, we might still expect the individual protostars to have a common angular momentum vector because of the overall velocity gradient observed in BHR71.

Using our knowledge of the envelope mass, we can calculate the Jeans length for BHR71 to determine if this is a feasible fragmentation mechanism. The Jeans length is approximately

$$\lambda_J = \frac{c_s}{\sqrt{G\rho}}, \quad (6)$$

where c_s is the sound speed (~ 0.25 km s $^{-1}$ for gas at 20 K), G is the gravitation constant, and ρ is the average density. We calculate the average density from the mass of $4.6 M_\odot$ that is estimated to be enclosed by a radius of 0.05 pc, which is $\sim 6 \times 10^{-19}$ g cm $^{-3}$ or $n \sim 10^5$ cm $^{-3}$. With these values, we estimate the Jeans length to be ~ 8400 au, which is much larger than the projected separation of IRS1 and IRS2. Lower temperatures were certainly possible prior to protostar formation (e.g., Stutz et al. 2010; Sadavoy et al. 2018) and higher densities as well, but an average density higher by ten times is necessary to make the Jeans length comparable to the current protostar separation. Thus, thermal Jeans fragmentation is not clearly a favored mechanism on its own to form the binary system, and turbulent fragmentation remains the most likely candidate.

5.3. Binary Arrangement along the Line of Sight

The structure of the core and relative positions of IRS1 and IRS2 along the line of sight is a source of uncertainty in the interpretation of the kinematics and companion formation. IRS2 appears to be either behind of or at the same distance with respect to IRS1 because the outflows do not appear to interact strongly. Such an interaction is expected to be accompanied by a shock, but *Spitzer* H_2 line mapping (Giannini et al. 2011) and *Herschel* [O I] mapping (Nisini et al. 2015) do not show strong emission at the location where the IRS2 outflow fans out. Moreover, the blueshifted lobe of IRS1 exits the globule, as seen in the infrared and optical imaging (e.g., Figure 1), so it may be near the front edge of the globule (at least not exactly in the center). Therefore IRS2, if it were even closer to us than IRS1, would be really close to the edge, but we see that it is very embedded and its blue lobe is not prominent in the near-infrared like that of IRS1.

The redshifted outflow from IRS2 does fan out on the southeast side of it, but this is not what would be expected if the outflow was interacting with the blueshifted outflow from IRS1. If the two outflows were interacting, the redshifted outflow from IRS2 would be expected to be deflected to the south, the direction of the blueshifted flow from IRS1. Since no such deflection is observed, the arrangement of the sources makes it unlikely that IRS2 is located in front of IRS1. The extension of the southeastern side of the redshifted outflow from IRS2 may more likely be related to how it is interacting with and exiting the core; outflows can also change their orientations over time as they accrete material with different angular momenta (Offner et al. 2016).

The C^{18}O velocities of IRS1 and IRS2 are approximately the same, as are the velocities of the NH_3 and N_2D^+ gas that is closely associated with these protostars. Thus, it is unlikely that they are within separate, but nearby cores along the line of sight, despite the second velocity component. With such an arrangement of IRS1 and IRS2, one could formulate a scenario where the actual separation of IRS1 and IRS2 is two to three times larger (if, e.g., IRS2 is located $\sim 6,000$ au behind IRS1), and assuming that IRS2 still orbits IRS1, the relative velocity of the protostars as measured by C^{18}O would be mostly tangential to the line of sight, causing their relative velocities to appear slower. We note, however, that regardless of how IRS1 and IRS2 are arranged in 3D, the opposite rotation directions for IRS1 and IRS2 are still inconsistent with rotation-induced fragmentation.

5.4. Future Observations to Characterize BHR71

While it has become somewhat cliché to suggest that further observations are needed to understand a particular system, we outline here a few specific missing pieces of the puzzle that would enable our ideas regarding fragmentation in BHR71 to be confirmed or ruled out.

First, the evidence for opposite rotation directions toward IRS1 and IRS2 in C^{18}O , which makes rotational fragmentation seem less likely, could be improved. A factor of 2–4 increases in both sensitivity and resolution would solidify this result. The present observations only have a resolution of $\sim 1''.5$, and the effective time on source for the protostars was only ~ 62 s on each mosaic point.

Second, the envelope kinematics on scales between the N_2D^+ and C^{18}O need improved resolution to better connect the kinematics from >1000 au scales to <1000 au scales where C^{18}O is the best tracer. Chen et al. (2008) published ATCA N_2H^+ observations that had severe limitations in sensitivity and spatial filtering. However, the regions traced in N_2H^+ are coincident with part of the N_2D^+ emission. Further observations of N_2H^+ with ALMA at high sensitivity and with coverage of both large and small spatial scales would further illuminate the likely opposite rotation of gas near the protostars. While NH_3 traces down to about the same scale as N_2H^+ and N_2D^+ , observations of NH_3 cannot currently be obtained at significantly higher resolution because of spatial filtering and the lower sensitivity of ATCA. Thus, N_2H^+ with ALMA is the best option going forward.

Third, higher sensitivity observations that could detect the NH_3 (2, 2) transition would be helpful in order to determine the gas kinetic temperature. However, higher sensitivity and resolution NH_3 observations are not trivial because ATCA is currently the only interferometer in the southern hemisphere

that can observe the NH_3 inversion transitions. Knowledge of the gas kinetic temperature could enable the susceptibility of the gas around the protostars to thermal Jeans fragmentation to be assessed. Such measurements of the kinetic temperature may also be possible using H_2CO (Mangum & Wootten 1993), however, if it is present in the envelope gas surrounding the protostars.

6. Summary and Conclusions

We have conducted a multiwavelength and multiline study of the isolated protobinary system located within BHR71 by unleashing a large battery of ground-based southern and space-based observatories on this system. We have resolved the two protostars IRS1 and IRS2 in the infrared out to $160\ \mu\text{m}$ using *Herschel* PACS photometry and conducted the most complete assessment of the SED toward IRS2. We also fully mapped the BHR71 core using *Herschel* SPIRE mapping. We have further characterized the continuum and kinematic properties of the envelope surrounding both sources, in addition to the individual envelopes around each of IRS1 and IRS2. This was done using ATCA and Parkes to observe NH_3 (1, 1) emission from the cold gas, and ALMA to image N_2D^+ and C^{18}O in addition to outflow tracers.

Our main results are as follows:

1. With observations that resolve the protostars out to $160\ \mu\text{m}$ and PSF photometry at $250\ \mu\text{m}$, we find that both are Class 0 protostars, as expected. IRS1 has a bolometric luminosity and temperature of $14.7\ L_\odot$ and $68\ \text{K}$, while IRS2 has values of $1.7\ L_\odot$ and $38\ \text{K}$. Thus, IRS2 could be less evolved than IRS1, but there are systematics related to source inclination that add uncertainty to T_{bol} .
2. We resolve the continuum emission toward each protostar at $1.3\ \text{mm}$ and $1.3\ \text{cm}$. We find that the radio spectra can be consistent with dust-only emission down to $1.3\ \text{cm}$ for both IRS1 and IRS2, even when the $3\ \text{mm}$ point from Chen et al. (2008) is included, but we cannot exclude some free-free emission at $1.3\ \text{cm}$. The total mass measured around the two protostars is $1.25\ M_\odot$, assuming a dust temperature of $20\ \text{K}$ for both protostars, and the masses of IRS1 and IRS2 individually are $1.13\ M_\odot$ and $0.11\ M_\odot$, respectively, with an assumed dust-to-gas mass ratio of 1:100 and Ossenkopf & Henning (1994) dust. If the dust temperature around IRS1 is $34\ \text{K}$, accounting for the higher luminosity, then the mass of IRS1 would be $0.59\ M_\odot$, making the combined mass $0.7\ M_\odot$. This continuum mass is a lower limit since there is substantially more cold dust surrounding the two protostars as viewed by *Herschel*. ALMA simply picks up the brightest emission close to each protostar. There is also weak evidence for a bridge of material between IRS1 and IRS2, perhaps similar to what is observed in IRAS 16293–2422 (Jacobsen et al. 2018).
3. The Parkes and ATCA observations seem to indicate a smooth velocity gradient across the core that could be interpreted as rotation. However, the ALMA N_2D^+ observations at higher resolution reveal a very complex velocity field that is not smooth. Position–velocity diagrams from both ALMA N_2D^+ and ATCA NH_3 find a second velocity component on the envelope east of IRS1. Some of this second component is likely to result

from the outflow influence on the envelope, but we also find that there is no clear velocity gradient across the envelope midplane from IRS1 to IRS2.

4. The ALMA observations also clearly detect ^{12}CO , ^{13}CO , and C^{18}O . ^{12}CO and ^{13}CO mainly trace the outflow emission from the protostars, while C^{18}O traces some emission along the outflow, but also the kinematics of the envelopes surrounding IRS1 and IRS2 on <1000 au scales. The C^{18}O velocities indicate that IRS1 and IRS2 are at the same velocity along the line of sight, so there is no evidence of orbital motion in their respective radial velocities. Moreover, the apparent rotation of the inner envelopes around IRS1 and IRS2 appear to be in the *opposite* directions!
5. We conclude that the binary formation in BHR71 is unlikely to have resulted from rotationally induced fragmentation of the core. The upper limit on the ratio of rotational energy to gravitational potential energy is low ($\beta_{\text{rot}} = 0.006$). This value is at the low end of the distribution presented in Chen et al. (2012). Furthermore, the N_2D^+ velocity field across IRS1 and IRS2, in the equatorial plane of the envelope, is consistent with no velocity gradient beyond the separation of the pair. There is no evidence of orbital motion given that the sources have the same systemic velocities along the line of sight, and the apparent rotation of the inner envelopes on scales smaller than 1000 au is in the opposite direction for IRS1 and IRS2. Thus, with all the evidence against ordered rotation leading to the formation of the binary system, we conclude that turbulent fragmentation might be the most likely formation scenario, given that the envelope has a velocity field that is not well ordered.

We acknowledge the constructive report from the anonymous referee that improved the quality of the manuscript. We also acknowledge useful discussions regarding BHR71 with M. Dunham and C. Hull, as well as help with *Starfinder* by N. Murillo. J.J.T. acknowledges support from NSF grant AST-1814762, the Homer L. Dodge Endowed Chair, and grant 639.041.439 from the Netherlands Organisation for Scientific Research (NWO). H.G.A. acknowledges the support of NSF grant AST-1714710. X.C. acknowledges support by the NSFC through grant 11473069. This paper makes use of the following

ALMA data: ADS/JAO.ALMA#2013.1.00518.S. ALMA is a partnership of ESO (representing its member states), NSF (USA) and NINS (Japan), together with NRC (Canada), NSC and ASIAA (Taiwan), and KASI (Republic of Korea), in cooperation with the Republic of Chile. The Joint ALMA Observatory is operated by ESO, AUI/NRAO and NAOJ. The National Radio Astronomy Observatory is a facility of the National Science Foundation operated under cooperative agreement by Associated Universities, Inc. This research made use of APLpy, an open-source plotting package for Python hosted at <http://aplpy.github.com>. This research made use of Astropy, a community-developed core Python package for Astronomy (Astropy Collaboration, 2013) <http://www.astropy.org>.

Facilities: ATCA, Parkes, ALMA, Herschel, Spitzer, CTIO(ISPI), Magellan (PANIC).

Software: Astropy (<http://www.astropy.org>; Astropy Collaboration et al. 2018; Greenfield et al. 2013), APLpy (<http://aplpy.github.com>; Robitaille & Bressert 2012), CASA (<http://casa.nrao.edu>; McMullin et al. 2007), The IDL Astronomy User's Library (<https://idlastro.gsfc.nasa.gov/>).

Appendix Hyperfine Fits

We show examples of the hyperfine fitting from CLASS for NH_3 and N_2D^+ in Figures 23 and 24. The fits show that there is evidence of a second component in some positions of the NH_3 and N_2D^+ velocity maps shown in Figures 10 and 16, respectively. The east side of the envelope in both NH_3 and N_2D^+ shows two components in Figures 12 and 17, respectively. These appear in the hyperfine fits as broader line width because a single-velocity component is adopted in the fitting process.

We further examined the issue of the second velocity component for the fit to the east side of the envelope, where the second component causes the most visible change to the line width (Figure 25). When we include a second component to the fit, we do find that the line widths are indeed smaller for each velocity component. We do not adopt a two-component fit for the entire envelope because the two-component fit often requires fine-tuning to obtain acceptable results. Thus a two-component fit cannot be used for the entire spectral cube.

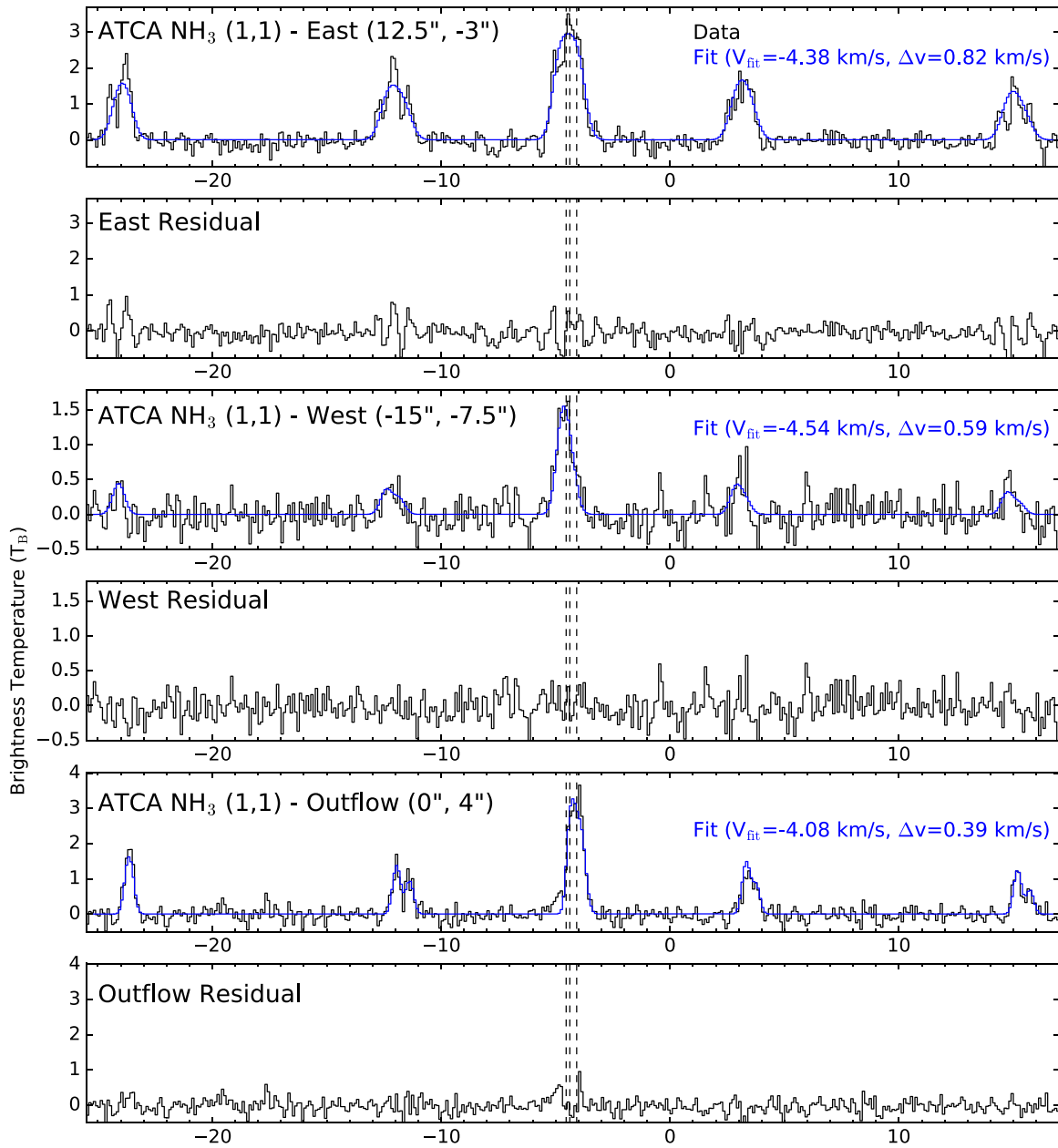


Figure 23. ATCA NH_3 spectra taken toward three positions, showing the spectrum and hyperfine fit in one panel and the residual of the fit below. The coordinates denoted for east, west, and outflow are relative to the position of IRS1 in Figure 10, and the extraction regions are also drawn as circles in the upper right panel of Figure 11. The east spectrum has the highest residual, which is likely due to the two velocity components that are apparent in Figure 14. The two blended components in the east spectrum cause a broader line width in the fit. The west and outflow positions are dominated by a single-velocity component; however, the outflow position has a low blueshifted residual.

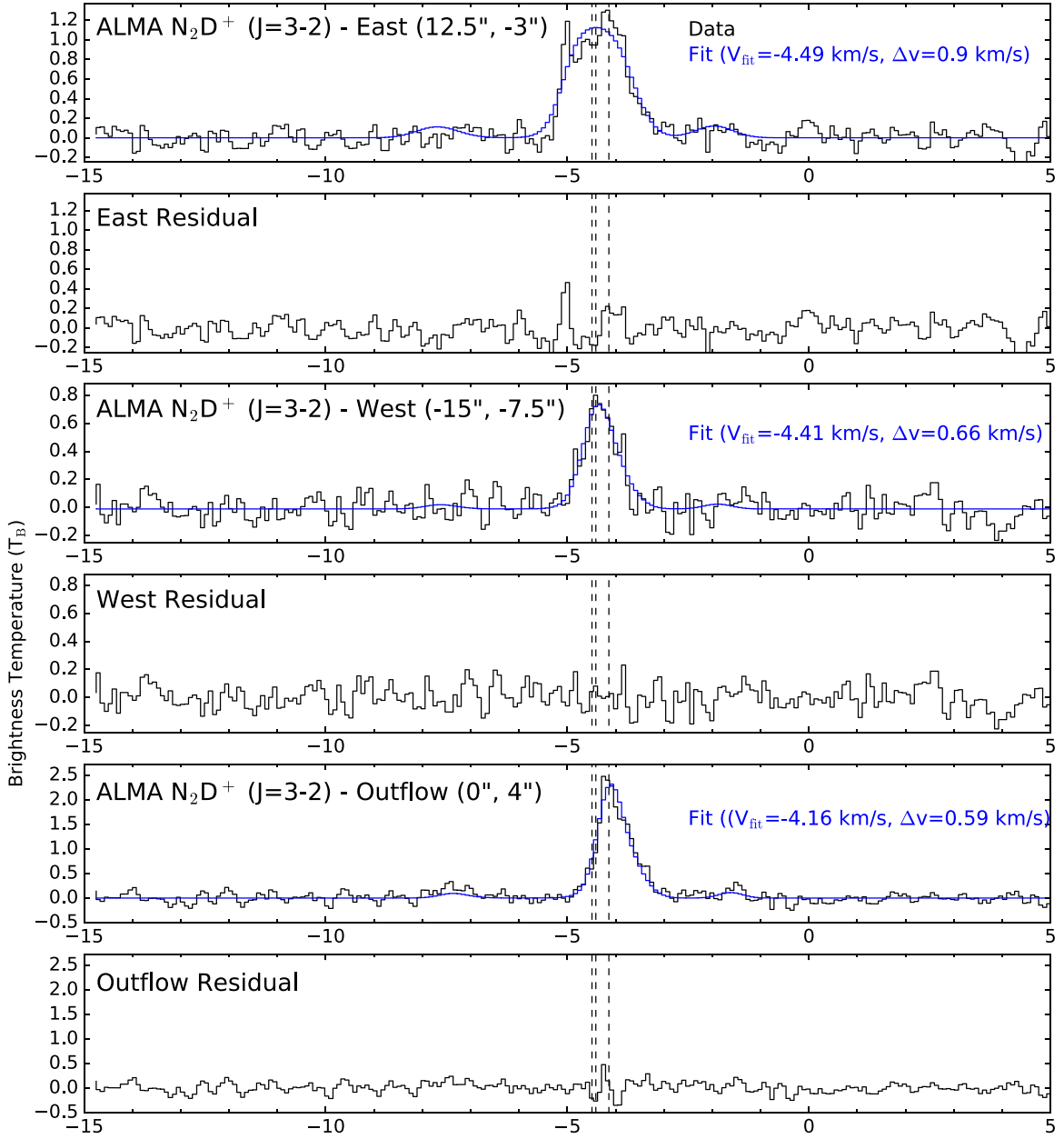


Figure 24. ALMA N_2D^+ spectra taken toward three positions, showing the spectrum and hyperfine fit in one panel and the residual of the fit below. The coordinates denoted for east, west, and outflow are relative to the position of IRS1 in Figure 16, and the extraction regions are also drawn as circles in the upper right panel of that Figure. The east spectrum has the highest residual, which is likely due to the two velocity components that are apparent in Figure 17. The two blended components in the east spectrum cause the broader line width in the fit. The west position is dominated by a single-velocity component, and the outflow position has a low residual.

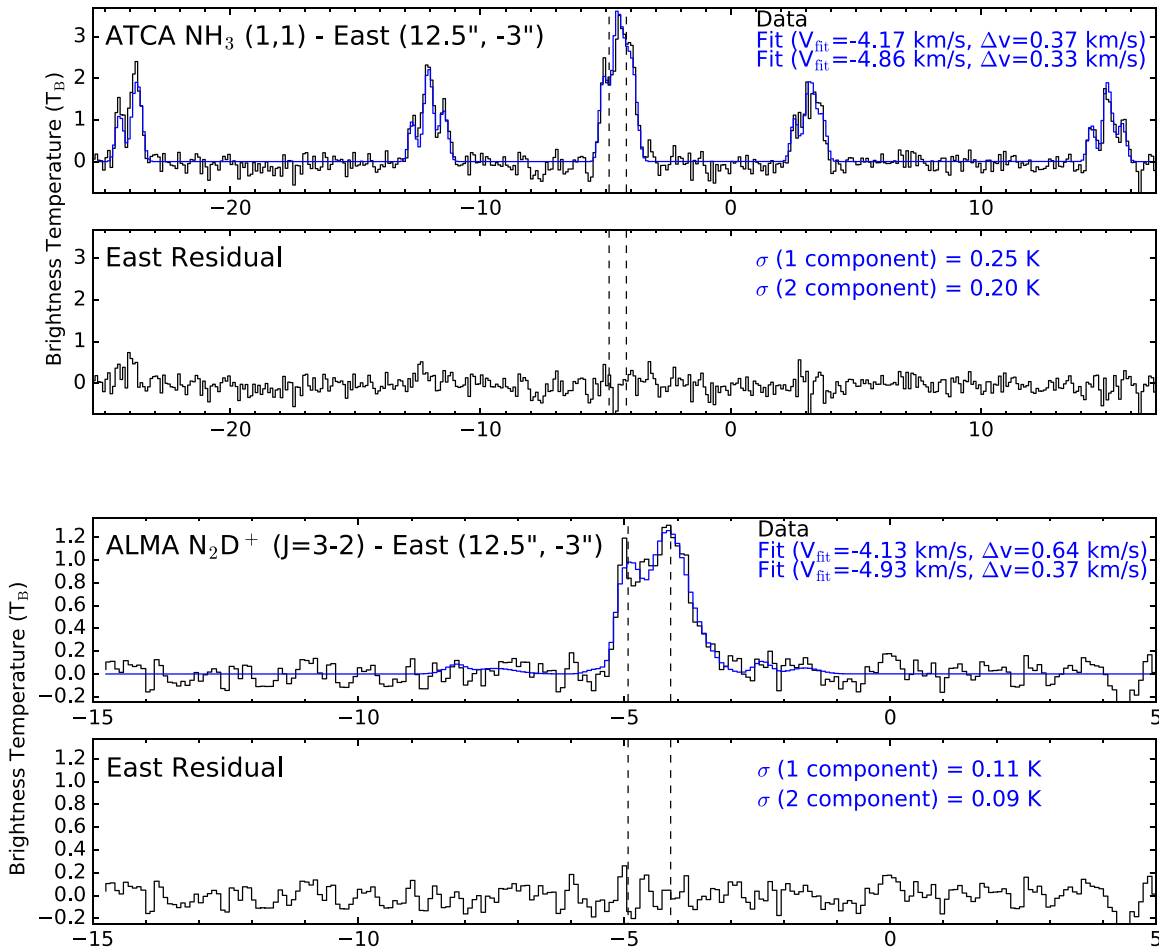


Figure 25. ALMA NH_3 and N_2D^+ spectra taken at the same east envelope position as in Figures 23 and 24. However, instead of a single-component fit, we attempt a two-component fit at this position to distinguish and characterize the two velocity components. The two-component fit is visually and statistically better than a single-component fit. The vertical dashed lines in both the upper and lower panels correspond to the central velocities of each component fit.

ORCID iDs

John J. Tobin <https://orcid.org/0000-0002-6195-0152>
 Lars Kristensen <https://orcid.org/0000-0003-1159-3721>
 Hector Arce <https://orcid.org/0000-0001-5653-7817>
 Claudio Codella <https://orcid.org/0000-0003-1514-3074>

References

- André, P., Men'shchikov, A., Bontemps, S., et al. 2010, *A&A*, **518**, L102
 André, P., Ward-Thompson, D., & Barsony, M. 1993, *ApJ*, **406**, 122
 Arce, H. G., & Sargent, A. I. 2006, *ApJ*, **646**, 1070
 Astropy Collaboration, Price-Whelan, A. M., Sipőcz, B. M., et al. 2018, *AJ*, **156**, 123
 Bate, M. R. 2012, *MNRAS*, **419**, 3115
 Benson, P. J., & Myers, P. C. 1989, *ApJS*, **71**, 89
 Bergin, E. A., Alves, J., Huard, T., & Lada, C. J. 2002, *ApJL*, **570**, L101
 Bohlin, R. C., Savage, B. D., & Drake, J. F. 1978, *ApJ*, **224**, 132
 Bonnell, I., & Bastien, P. 1993, *ApJ*, **406**, 614
 Boss, A. P. 1995, *RMxAC*, **1**, 165
 Boss, A. P. 2002, *ApJ*, **568**, 743
 Boss, A. P., & Bodenheimer, P. 1979, *ApJ*, **234**, 289
 Boss, A. P., & Keiser, S. A. 2013, *ApJ*, **764**, 136
 Boss, A. P., & Keiser, S. A. 2014, *ApJ*, **794**, 44
 Bourke, T. L. 2001, *ApJL*, **554**, L91
 Bourke, T. L., Hyland, A. R., & Robinson, G. 1995a, *MNRAS*, **276**, 1052
 Bourke, T. L., Hyland, A. R., Robinson, G., James, S. D., & Wright, C. M. 1995b, *MNRAS*, **276**, 1067
 Brinch, C., Jørgensen, J. K., Hogerheijde, M. R., Nelson, R. P., & Gressel, O. 2016, *ApJL*, **830**, L16
 Burkert, A., & Bodenheimer, P. 1993, *MNRAS*, **264**, 798
 Caselli, P., Benson, P. J., Myers, P. C., & Tafalla, M. 2002, *ApJ*, **572**, 238
 Chen, H., Myers, P. C., Ladd, E. F., & Wood, D. O. S. 1995, *ApJ*, **445**, 377
 Chen, X., Arce, H. G., Dunham, M. M., & Zhang, Q. 2012, *ApJL*, **747**, L43
 Chen, X., Arce, H. G., Zhang, Q., et al. 2013, *ApJ*, **768**, 110
 Chen, X., Launhardt, R., Bourke, T. L., Henning, T., & Barnes, P. J. 2008, *ApJ*, **683**, 862
 Chen, X., Launhardt, R., & Henning, T. 2007, *ApJ*, **669**, 1058
 Chiang, H., Looney, L. W., & Tobin, J. J. 2012, *ApJ*, **709**, 470
 Diolaiti, E., Bendinelli, O., Bonaccini, D., et al. 2000, *Proc. SPIE*, **4007**, 879
 Dore, L., Caselli, P., Beninati, S., et al. 2004, *A&A*, **413**, 1177
 Drabek, E., Hatchell, J., Friberg, P., et al. 2012, *MNRAS*, **426**, 23
 Duchêne, G., & Kraus, A. 2013, *ARA&A*, **51**, 269
 Dunham, M. M., Stutz, A. M., Allen, L. E., et al. 2014, in *Protostars and Planets VI*, ed. H. Beuther et al. (Tucson, AZ: Univ. Arizona Press), **195**
 Fazio, G. G., Hora, J. L., Allen, L. E., et al. 2004, *ApJS*, **154**, 10
 Frerking, M. A., Langer, W. D., & Wilson, R. W. 1982, *ApJ*, **262**, 590
 Furlan, E., Fischer, W. J., Ali, B., et al. 2016, *ApJS*, **224**, 5
 Giannini, T., Nisini, B., Neufeld, D., et al. 2011, *ApJ*, **738**, 80
 Goodman, A. A., Benson, P. J., Fuller, G. A., & Myers, P. C. 1993, *ApJ*, **406**, 528
 Goodwin, S. P., Whitworth, A. P., & Ward-Thompson, D. 2004, *A&A*, **414**, 633
 Greenfield, P., Robitaille, T., Tollerud, E., et al. 2013, Astropy: Community Python Library for Astronomy, ascl:1304.002
 Griffin, M. J., Abergel, A., Abreu, A., et al. 2010, *A&A*, **518**, L3
 Hacar, A., & Tafalla, M. 2011, *A&A*, **533**, A34
 Herbst, E. 1982, *A&A*, **111**, 76
 Houck, J. R., Roellig, T. L., van Cleve, J., et al. 2004, *ApJS*, **154**, 18
 Jacobsen, S. K., Jørgensen, J. K., van der Wiel, M. H. D., et al. 2018, *A&A*, **612**, A72
 Jensen, E. L. N., & Akeson, R. 2014, *Natur*, **511**, 567

- Johnstone, D., Rosolowsky, E., Tafalla, M., & Kirk, H. 2010, *ApJ*, **711**, 655
- Krasnopolsky, R., Li, Z.-Y., & Shang, H. 2010, *ApJ*, **716**, 1541
- Kraus, A. L., Ireland, M. J., Martinache, F., & Hillenbrand, L. A. 2011, *ApJ*, **731**, 8
- Kwon, W., Looney, L. W., Mundy, L. G., Chiang, H.-F., & Kembell, A. J. 2009, *ApJ*, **696**, 841
- Lada, C. J., & Lada, E. A. 2003, *ARA&A*, **41**, 57
- Ladd, E. F., Adams, F. C., Fuller, G. A., et al. 1991, *ApJ*, **382**, 555
- Larson, R. B. 1972, *MNRAS*, **156**, 437
- Launhardt, R., Nutter, D., Ward-Thompson, D., et al. 2010, *ApJS*, **188**, 139
- Lee, J., Bergin, E. A., & Evans, N. J., II 2004, *ApJ*, **617**, 360
- Lee, J.-E., Lee, S., Dunham, M. M., et al. 2017, *NatAs*, **1**, 0172
- Lee, K. I., Dunham, M. M., Myers, P. C., et al. 2016, *ApJL*, **820**, L2
- Looney, L. W., Tobin, J. J., & Kwon, W. 2007, *ApJL*, **670**, L131
- Machida, M. N., Tomisaka, K., Matsumoto, T., & Inutsuka, S. 2008, *ApJ*, **677**, 327
- Magnelli, B., Popesso, P., Berta, S., et al. 2013, *A&A*, **553**, A132
- Mangum, J. G., & Wootten, A. 1993, *ApJS*, **89**, 123
- Martini, P., Persson, S. E., Murphy, D. C., et al. 2004, *Proc. SPIE*, **5492**, 1653
- McMullin, J. P., Waters, B., Schiebel, D., Young, W., & Golap, K. 2007, in ASP Conf. Ser. 376, *Astronomical Data Analysis Software and Systems XVI*, ed. R. A. Shaw, F. Hill, & D. J. Bell (San Francisco, CA: ASP), 127
- Megeath, S. T., Gutermuth, R., Muzerolle, J., et al. 2012, *AJ*, **144**, 192
- Myers, P. C., Adams, F. C., Chen, H., & Schaff, E. 1998, *ApJ*, **492**, 703
- Myers, P. C., & Ladd, E. F. 1993, *ApJL*, **413**, L47
- Nisini, B., Santangelo, G., Giannini, T., et al. 2015, *ApJ*, **801**, 121
- Offner, S. S. R., & Arce, H. G. 2014, *ApJ*, **784**, 61
- Offner, S. S. R., Dunham, M. M., Lee, K. I., Arce, H. G., & Fielding, D. B. 2016, *ApJL*, **827**, L11
- Offner, S. S. R., Kratter, K. M., Matzner, C. D., Krumholz, M. R., & Klein, R. I. 2010, *ApJ*, **725**, 1485
- Ossenkopf, V., & Henning, T. 1994, *A&A*, **291**, 943
- Padoan, P., & Nordlund, A. 2002, *ApJ*, **576**, 870
- Parise, B., Belloche, A., Leurini, S., et al. 2006, *A&A*, **454**, L79
- Pineda, J. E., Offner, S. S. R., Parker, R. J., et al. 2015, *Natur*, **518**, 213
- Poglitsch, A., Waelkens, C., Geis, N., et al. 2010, *A&A*, **518**, L2
- Price, D. J., & Bate, M. R. 2007, *MNRAS*, **377**, 77
- Raghavan, D., McAlister, H. A., Henry, T. J., et al. 2010, *ApJS*, **190**, 1
- Rieke, G. H., Young, E. T., Engelbracht, C. W., et al. 2004, *ApJS*, **154**, 25
- Robitaille, T., & Bressert, E. 2012, *APLpy: Astronomical Plotting Library in Python*, Astrophysics Source Code Library, ascl:1208.017
- Roussel, H. 2013, *PASP*, **125**, 1126
- Sadavoy, S. I., Keto, E., Bourke, T. L., et al. 2018, *ApJ*, **852**, 102
- Sault, R. J., Teuben, P. J., & Wright, M. C. H. 1995, in ASP Conf. Ser. 77, *Astronomical Data Analysis Software and Systems IV*, ed. R. A. Shaw, H. E. Payne, & J. J. E. Hayes (San Francisco, CA: ASP), 433
- Shu, F. H. 1977, *ApJ*, **214**, 488
- Skrutskie, M. F., Cutri, R. M., Stiening, R., et al. 2006, *AJ*, **131**, 1163
- Stapelfeldt, K. R., Ménard, F., Watson, A. M., et al. 2003, *ApJ*, **589**, 410
- Stutz, A., Launhardt, R., Linz, H., et al. 2010, *A&A*, **518**, L87
- Terebey, S., Shu, F. H., & Cassen, P. 1984, *ApJ*, **286**, 529
- Tobin, J. J., Bergin, E. A., Hartmann, L., et al. 2013, *ApJ*, **765**, 18
- Tobin, J. J., Bos, S. P., Dunham, M. M., Bourke, T. L., & van der Marel, N. 2018, *ApJ*, **856**, 164
- Tobin, J. J., Hartmann, L., Bergin, E., et al. 2012a, *ApJ*, **748**, 16
- Tobin, J. J., Hartmann, L., Chiang, H.-F., et al. 2011, *ApJ*, **740**, 45
- Tobin, J. J., Hartmann, L., Chiang, H.-F., et al. 2012b, *Natur*, **492**, 83
- Tobin, J. J., Hartmann, L., Looney, L. W., & Chiang, H. 2010a, *ApJ*, **712**, 1010
- Tobin, J. J., Hartmann, L., Looney, L. W., & Chiang, H.-F. 2010b, *ApJ*, **712**, 1010
- Tobin, J. J., Looney, L. W., Li, Z.-Y., et al. 2016, *ApJ*, **818**, 73
- Tohline, J. E. 2002, *ARA&A*, **40**, 349
- Tsukamoto, Y., Iwasaki, K., Okuzumi, S., Machida, M. N., & Inutsuka, S. 2015, *ApJL*, **810**, L26
- van der Blik, N. S., Norman, D., Blum, R. D., et al. 2004, *Proc. SPIE*, **5492**, 1582
- Visser, R., Doty, S. D., & van Dishoeck, E. F. 2011, *A&A*, **534**, A132
- Walch, S., Naab, T., Whitworth, A., Burkert, A., & Gritschneider, M. 2010, *MNRAS*, **402**, 2253
- Walch, S., Whitworth, A. P., & Girichidis, P. 2012, *MNRAS*, **419**, 760
- Ward-Duong, K., Patience, J., De Rosa, R. J., et al. 2015, *MNRAS*, **449**, 2618
- Whitney, B. A., Wood, K., Bjorkman, J. E., & Wolff, M. J. 2003, *ApJ*, **591**, 1049
- Williams, J. P., Mann, R. K., Di Francesco, J., et al. 2014, *ApJ*, arXiv:1410.3570
- Yang, Y.-L., Evans, N. J., II, Green, J. D., Dunham, M. M., & Jørgensen, J. K. 2017, *ApJ*, **835**, 259
- Yen, H.-W., Takakuwa, S., Ohashi, N., & Ho, P. T. P. 2013, *ApJ*, **772**, 22
- Zapata, L. A., Loinard, L., Rodríguez, L. F., et al. 2013, *ApJL*, **764**, L14